Research Article
Open Access

A systems-level computational analysis of UVA-responsive hyaluronic acid and ascorbic acid interactomes and ligand–protein interactions in human skin

Abstract

Environmental stress does not uniformly disrupt biological systems but instead induces selective reorganization of regulatory networks. What extracellular matrix dynamics and intracellular redox systems are co-ordinately rewired under stress remains poorly defined. Here, we apply a UVA-regulated hub-centred network analysis to resolve UVA-induced coupling between hyaluronic acid (HA)–associated extracellular signalling and ascorbic acid (AA)–associated intracellular redox networks in human skin. Integration of curated HA and AA interactomes with UVA-responsive transcriptomic data (GEO accession GSE240226; UVA-irradiated versus untreated primary human dermal fibroblasts, n = 3 per group) shows that differentially expressed genes (DEGs) occupy positions of significantly higher topological centrality than non-responsive nodes in the HA interactome and in the integrated HA–AA network (Mann–Whitney U test and 10,000-fold label-permutation testing, $p < 0.01$ for degree, betweenness, closeness, stress and radiality), whereas no such enrichment was detected in the AA interactome ($p > 0.05$). This asymmetry is dominated by HA-centred inflammatory and matrix-regulatory nodes and modulated by AA-associated redox and transport proteins. Structure-based docking predicts oligomer length–dependent differences in HA receptor compatibility: CD44 returned favourable docking scores for the shorter oligomers HA4 and HA6 but unfavourable scores for HA8, whereas LYVE1 retained favourable scores across all three oligomer lengths tested. These are predictions of structural compatibility and are not measurements of binding affinity or receptor selectivity. In parallel, the cytosolic redox effectors CLIC1 and GSTO1 — selected on functional and biochemical grounds rather than on network centrality, and which were neither consensus hubs nor DEGs in this analysis — returned favourable predicted docking with dehydroascorbate, as did the UVA-downregulated transporters SLC2A3 and SLC2A14. Together, these findings propose a systems-level framework linking extracellular matrix signalling and intracellular redox regulation during UVA stress. This is an entirely in silico, hypothesis-generating study: it prioritises candidate molecules linking HA- and AA-associated pathways for subsequent experimental testing, but the candidates reported here are computational predictions and are not proposed as validated biomarkers or therapeutic targets.

Keywords: UVA stress, hyaluronic acid signalling, ascorbic acid redox metabolism, hub-centred network analysis, extracellular–intracellular coupling

Volume 14 Issue 3 - 2026

Krittika Ghatak, Kirti Rani
Amity Institute of Biotechnology, Amity University Uttar Pradesh, India

Correspondence: Dr. Kirti Rani, Associate Professor, Amity Institute of Biotechnology, Amity University Uttar Pradesh, Noida, Sec-125, Gautam Buddha Nagar, Noida (City)-201313 (UP), India. Mobile No: +91-9990329492

Received: August 22, 2026 | **Published:** September 29, 2026

Introduction

UVA-induced skin stress

The human body experiences constant ultraviolet (UV) radiation exposure which makes its skin the most environmentally damaged organ in the body. The biological functions of the skin are disrupted by continuous or excessive ultraviolet light exposure which affects the organization of extracellular matrix components, the control of redox balance inside cells, the process of immune system monitoring, and the mechanisms that maintain skin health, which eventually leads to skin aging, disease, and cancer development. The skin experiences two types of damage from UV radiation: direct molecular harm and indirect oxidative stress that occurs when reactive oxygen species (ROS) are produced, which activates signalling pathways that result in changes to gene expression and protein interactions and tissue structure. Skin stress responses develop through systems that govern both extracellular and intracellular elements which work together to maintain skin health. Scientists must study UV radiation effects on biological networks through system-wide methods which analyse multiple molecular pathways instead of studying particular molecules or pathways.

Hyaluronic acid biology and extracellular matrix remodelling

Hyaluronan (HA), also known as hyaluronic acid, is a **highly dynamic glycosaminoglycan (GAG)** ubiquitously present in the extracellular matrix (ECM) of vertebrate tissues. It is a linear polymer composed of repeating disaccharides of D-glucuronic acid and N-acetyl-D-glucosamine linked by β1→4 and β1→3 bonds[1] and represents approximately 50 % of total body HA, and modulates keratinocyte proliferation, differentiation, and barrier function via interactions with canonical HA receptors such as CD44, RHAMM (HMMR), and LYVE-1.[2,3] Importantly, HA turnover in the skin is rapid, with a half-life of less than a day, managed by hyaluronan synthases (HAS1-3) and degradative pathways like hyaluronidases and ROS-triggered mechanisms.[4,5] The *molecular weight (MW)* of HA dictates its biological actions as its chain length determines its physical structure or viscoelasticity. High-molecular-weight

Submit Manuscript | http://medcraveonline.com

©2026 Ghatak et al. This is an open access article distributed under the terms of the Creative Commons Attribution License, which permits unrestricted use, distribution, and build upon your work non-commercially.

HA (HMW-HA; >1 × 10^6 Da) promotes anti-inflammatory and hydrating effects, while low-molecular-weight HA (LMW-HA) and oligosaccharides can activate innate immune receptors such as TLR2, TLR4, and CD44, leading to pro-inflammatory signals and altered cellular migration.[6,7] HA fragmentation is not merely a biochemical by-product but a functional switch in tissue stress, inflammation, and repair. For example, LMW-HA accumulates in photoaged human skin and is associated with decreased HAS expression and increased HYAL activities after UV exposure, suggesting that UV-induced oxidative stress shifts HA homeostasis toward catabolic states that impact tissue hydration, matrix integrity, and receptor engagement.[8]

Ascorbic acid and cutaneous redox biology

Importantly, ultraviolet-induced skin damage does not act on extracellular matrix components in isolation but simultaneously perturbs intracellular redox homeostasis and antioxidant defence systems. UV-driven oxidative stress that accelerates hyaluronan fragmentation also consumes endogenous antioxidants, creating a coupled extracellular–intracellular stress landscape. Despite their biological interdependence, these two systems are typically studied independently, leaving a critical gap in understanding how UV stress co-ordinately rewires ECM-associated signalling networks and intracellular antioxidant machinery. Ascorbic acid (vitamin C, AA) is a small, water-soluble antioxidant and essential cofactor that plays pivotal roles in human skin physiology, including collagen synthesis, redox homeostasis, keratinocyte differentiation, and pigmentation control, all processes that are directly perturbed by ultraviolet (UV) irradiation. Under UV-induced oxidative stress, intracellular AA is rapidly oxidized to dehydroascorbic acid (DHA), which represents a dominant transient redox state and is actively transported via glucose transporters before enzymatic recycling to ascorbate. Accordingly, DHA constitutes a physiologically relevant ligand for interrogating vitamin C–dependent protein interactions and signalling events under UV stress conditions. AA cannot be synthesized endogenously in humans due to loss of L-gulono-γ-lactone oxidase activity, and thus must be acquired from diet or topical application.[9] Vitamin C is also the predominant non-enzymatic antioxidant in the skin, found at high concentrations in both the epidermis and dermis, where it functions to neutralize ROS generated by UVA/UVB exposure.[10] UVA produces singlet oxygen and free radicals, while UVB causes thymine dimer formation and additional oxidative cascades.[11] Excessive UV exposure depletes AA levels in the epidermis in an intensity- and duration-dependent manner, creating a local deficiency of this critical antioxidant precisely where it is most needed.[12] At the molecular level, AA suppresses UVB-induced ROS, protects against DNA damage and apoptosis, and downregulates pro-inflammatory cytokine expression, including TNF-α, in human epidermal models.[13] In vitro studies confirm that AA partially prevents UV-induced redox imbalance in human fibroblasts exposed to UVA/UVB, inhibiting lipid peroxidation and maintaining antioxidant enzyme activity, although protection of macromolecules such as DNA is only partial.[14]

Knowledge gaps

However, many studies investigating UV-induced skin aging emphasise global changes in HA content, molecular weight distribution, or dermal architecture, while providing limited mechanistic resolution of how HA fragmentation dynamically alters receptor-specific signalling networks under stress conditions.[4,8,15-17] Although UVB exposure is known to downregulate HA synthases and accelerate HA degradation in both epidermal and dermal compartments, these processes are often examined independently from downstream receptor engagement and signalling consequences.[18-20] CD44-mediated HA signalling has been extensively characterized in inflammation, wound repair, and cancer biology, yet comparatively fewer PubMed-indexed studies explore how UV-induced HA fragmentation modulates CD44 signalling specificity versus alternative receptors such as RHAMM or LYVE-1.[21-25] Existing studies often rely on simplified in vitro systems or isolated cell types, which do not fully capture the multicellular complexity of skin, including immune, vascular, and lymphatic components critical for HA-mediated homeostasis.[26] Additionally, although oxidative stress and matrix remodelling are recognized as central drivers of HA turnover and receptor activation during aging, few investigations integrate redox signalling, HA metabolism, and receptor interact omics into unified systems-level frameworks.[27-29] Longitudinal human studies addressing how chronic UV exposure reshapes HA–receptor networks over time are particularly limited, constraining translational relevance for therapeutic targeting and biomaterial design.[30] Similarly, AA-related studies exhibit critical mechanistic gaps. Most studies examine gross antioxidant outcomes or histological markers, often using multi-component mixtures that confound attribution of effects specifically to AA, and with little resolution of how AA interacts with specific cutaneous receptors or redox-sensitive signalling pathways (e.g., Nrf2, AP-1, NF-κB) under UV stress.[31-33] The dynamics of AA transport (e.g., via SVCT1/2) in keratinocytes and fibroblasts under UV stress and how this affects intracellular signalling, gene expression, and antioxidant network compensation remain underexplored.[9,34] Furthermore, the oxidized metabolites of AA (e.g., dehydroascorbic acid) and their biological activities during or after UV exposure are poorly integrated into current models.[35-38]

Study objective and hypothesis

Taken together, hyaluronan-driven extracellular signalling and ascorbic acid–mediated intracellular redox control constitute two complementary yet interconnected response systems governing skin resilience under ultraviolet stress. HA fragmentation alters receptor engagement, immune activation, and matrix organisation, while concurrent AA depletion and DHA accumulation reshape intracellular antioxidant capacity and redox-sensitive signalling pathways. Both processes converge on shared biological outcomes, including inflammation, impaired repair, altered cell migration, and dysregulated stress adaptation. However, the extent to which these systems are co-ordinately regulated at the network level under UV exposure remains poorly defined. To address these critical gaps, the research study involves the implementation of a comprehensive computational and systems-based research framework which starts with complete identification of extracellular matrix and antioxidant-related proteins through approved biological databases and high-trust chemical-to-protein interaction databases and proceeds to network analysis which reveals functional patterns and vital control centres. The study combines interactome data with UVA-dependent gene expression information to determine which proteins show changes in both their expression levels and their network relationships when exposed to ultraviolet light, thus demonstrating how their protective mechanisms change according to different environmental situations. To avoid arbitrary target selection, the study applies strict ontology-driven prioritization to isolate biologically relevant ligand-binding proteins and redox-associated interactors, ensuring mechanistic relevance of downstream analyses. Collectively, this integrated approach enables a mechanistically grounded dissection of how ultraviolet stress co-ordinately perturbs extracellular matrix signalling and intracellular redox regulation, providing insight into skin stress responses and informing the rational design of therapeutic and biomaterial strategies aimed at enhancing cutaneous resilience to UVA irradiation.

Citation: Ghatak K, Rani K. A systems-level computational analysis of UVA-responsive hyaluronic acid and ascorbic acid interactomes and ligand–protein interactions in human skin. *J Bacteriol Mycol Open Access.* 2026;14(3):88–108. DOI: 10.15406/jbmoa.2026.14.00435

On this basis we tested three explicit predictions. First, if UVA stress is accommodated through a structured rather than a diffuse reorganisation of the cutaneous molecular network, then UVA-responsive genes should occupy positions of significantly higher topological centrality than non-responsive genes within the curated HA- and AA-associated interactomes. Second, because HA-associated signalling is extracellular, matrix-facing and densely interconnected whereas AA-associated biology is intracellular, enzymatic and comparatively modular, the two arms should contribute asymmetrically to the integrated network, with HA-derived nodes dominating consensus hub membership. Third, if HA fragment size governs receptor engagement, then HA receptors should differ in their predicted structural compatibility with short versus long HA oligomers. These three predictions are addressed below by permutation-based centrality statistics, consensus hub overlap analysis, and structure-based molecular docking, respectively. Because every component of this study is computational, all outcomes are treated throughout as hypotheses requiring experimental validation rather than as demonstrated mechanisms.

Materials and methodology

Identification of ascorbic acid and hyaluronic acid-associated human proteins

Hyaluronic acid–associated human protein targets were identified through a combined database mining approach using UniProtKB[39] and STITCH (v5.0).[40] UniProtKB was queried using the keywords "hyaluronic acid", "hyaluronan", "hyaluronan receptor", "hyaluronan binding" and "hyaluronan metabolic process". Ascorbic acid–associated human protein targets were identified through the same approach and queried using the keywords "vitamin C", "ascorbate", "ascorbate transporter", and "ascorbic acid". Searches were restricted to reviewed (Swiss-Prot) entries and Homo sapiens only to ensure high annotation quality. The combined keyword-based search retrieved 138 human proteins (including duplicates) for HA and 200 human proteins (with duplicates) for AA from UniProtKB. In parallel, chemical–protein interaction data were obtained from the STITCH database (Figure 1), using hyaluronan and, as a separate and independent query, ascorbic acid as query compounds. Interactions were restricted to Homo sapiens, and only interactions with a confidence score > 0.4 were retained, yielding 10 and 9 proteins for HA and AA respectively. Protein lists from UniProtKB and STITCH were merged, standardized to UniProt accession numbers, and manually inspected. Duplicate entries across sources were removed, resulting in a final set of 88 non-redundant, high-confidence hyaluronic acid–associated human proteins, and 90 ascorbic acid-associated proteins, which was used for all downstream analyses.

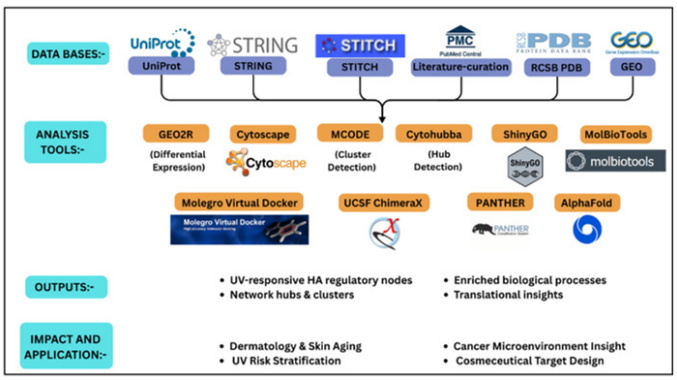

Figure 1 Schematic overview of the integrative network and structural bioinformatics workflow used in this study. The methodological design was conceptually inspired and adapted from a previously published framework,[41] with additional tools, analyses, and extensions incorporated to address the specific objectives of the present work.

Search reproducibility and exclusion criteria. All queries were restricted to Homo sapiens (organism_id: 9606) and, for UniProtKB, to reviewed (Swiss-Prot) entries. The complete query strings were: for HA, ("hyaluronic acid" OR "hyaluronan" OR "hyaluronan receptor" OR "hyaluronan binding" OR "hyaluronan metabolic process") AND organism_id:9606 AND reviewed:true; and for AA, ("vitamin C" OR "ascorbate" OR "ascorbate transporter" OR "ascorbic acid") AND organism_id:9606 AND reviewed:true. Both databases were accessed on [AUTHORS: INSERT EXACT SEARCH DATE(S)]. Entries were excluded if they were unreviewed, non-human, or annotated to the query terms only by electronic inference without a supporting hyaluronan- or ascorbate-related Gene Ontology term. Duplicate entries arising from overlapping keyword hits and from the UniProtKB–STITCH merge were removed at the level of the UniProt accession, retaining a single canonical entry per gene. This procedure yielded 88 HA-associated and 90 AA-associated non-redundant proteins. The complete annotated protein lists, with UniProt accessions, gene symbols, source database and STITCH confidence scores where applicable, are provided in Supplementary Table S1.[41]

Transcriptomic analysis and DEG-mapped network construction of HA and AA interactomes

Protein–protein interaction (PPI) network construction was performed using the STRING database (v12).[42] The curated hyaluronic acid–associated and ascorbic acid–associated protein lists were uploaded as two separate, independent STRING queries, each with the species set to Homo sapiens and with identical parameters applied to both. The integrated HA–AA network was then constructed by submitting the union of the two curated lists (177 non-redundant proteins; CFTR was the single protein common to both lists) to STRING under the same settings. Active interaction sources were restricted to Experiments and Databases; all remaining STRING evidence channels — Text mining, Gene Neighbourhood, Gene Fusion, Co-occurrence and Co-expression — were disabled. A minimum required interaction score of 0.400 (medium confidence) was applied, and the maximum number of additional interactors was set to zero for both the first and the second shell, so that no proteins outside the curated input lists were added to any network. The resulting interaction network was imported into Cytoscape (v3.10.3)[43] for visualization and downstream network analyses. To integrate ultraviolet (UVA) exposure relevance, a publicly available Gene Expression Omnibus (GEO)[44] dataset GSE240226 was retrieved. This series (platform GPL24676, Illumina NovaSeq 6000; Homo sapiens; expression profiling by high-throughput RNA sequencing) comprises 12 samples of primary human dermal fibroblasts (HDFs) isolated from human skin dermis and used between passages 5 and 15, distributed across four experimental groups of three biological replicates each: untreated control (GSM7688465–GSM7688467), UVA alone (GSM7688468–GSM7688470), Maifuyin + UVA (GSM7688471–GSM7688473) and succinic acid + UVA (GSM7688474–GSM7688476). In the originating study, cells were washed, resuspended in PBS, irradiated with a single dose of 2 J/cm² UVA (controls were handled identically but left unirradiated) and then incubated in fresh serum-free medium for 3 h before RNA extraction. Only the UVA-alone versus untreated-control contrast (n = 3 per group) was used in the present work; the two ingredient-treated arms were not analysed. Differential expression was assessed with GEO2R, which for RNA-sequencing series applies the DESeq2 pipeline to the NCBI-generated raw count matrix, with Benjamini–Hochberg control of the false discovery rate. Genes were

called differentially expressed at the GEO2R significance cut-off of a Benjamini–Hochberg adjusted p-value < 0.05, with a $\log_2$ fold-change cut-off of [AUTHORS: STATE THE |log2FC| THRESHOLD APPLIED, OR "none" IF NO FOLD-CHANGE FILTER WAS USED]. The complete DEG list with $\log_2$ fold-change and adjusted p-values is provided in Supplementary Table S2. The resulting DEG list was intersected with the curated HA and AA protein lists using the MolBioTools[45] Multiple List Comparator, which was used exclusively for set comparison and Venn diagram visualisation and performed no statistical testing, normalisation or network mapping of its own. The intersecting genes were then mapped onto the HA, AA and integrated PPI networks within Cytoscape to generate the UVA-integrated interaction networks.

Network topology and statistical testing. Topological parameters of each network (number of nodes and edges, average node degree, average clustering coefficient, number of disconnected nodes and number of connected components) were computed in Cytoscape using the NetworkAnalyzer tool, treating all edges as undirected and excluding self-loops; these values are reported in Table 1. To test formally whether UVA-responsive genes occupy more central network positions than non-responsive genes — rather than inferring this from visual inspection — the distribution of each centrality metric (degree, betweenness, closeness, stress and radiality) was compared between DEG and non-DEG nodes within each network using the one-sided Mann–Whitney U test, with the rank-biserial correlation reported as a distribution-free effect size. Each comparison was additionally evaluated by a label-permutation test in which DEG labels were randomly reassigned across all nodes of the network 10,000 times and the observed mean centrality of the DEG set was compared against the resulting null distribution. Analyses were performed in Python 3.12 (SciPy v1.16, NumPy v2.2) with a fixed random seed for reproducibility; nodes with undefined radiality (isolated nodes) were excluded from the radiality comparison only.

Functional classification of HA- and AA-associated proteins

Protein classification analysis was performed using the Protein Analysis Through Evolutionary Relationships (PANTHER) (v19.0) Classification System.[46] The complete integrated set of hyaluronic acid–associated and ascorbic acid–associated proteins were analysed to determine protein family classifications. Classification was based on evolutionary relationships, allowing proteins to be grouped into defined families and classes represented within the dataset.

Network topological analysis and hub identification

Topological analysis of the UVA-integrated PPI network was performed in Cytoscape using the cytoHubba (v0.1)[47] plugin. Five centrality algorithms were applied to identify key regulatory proteins: Maximal Clique Centrality (MCC), Density of Maximum Neighbourhood Component (DMNC), Edge Percolated Component (EPC), Radiality centrality and Stress centrality. For each method, proteins were ranked based on their centrality scores. A consensus hub selection strategy was employed to reduce method-specific bias. Proteins appearing in the top 10 rankings of at least two of the five centrality methods were defined as consensus hub proteins. This rule follows the widely used convention of requiring agreement between independent centrality algorithms rather than relying on any single ranking, and the two-of-five threshold was adopted because each algorithm emphasises a different topological property (local clique structure for MCC, neighbourhood density for DMNC, percolation robustness for EPC, and global path structure for radiality and stress), so that agreement between any two algorithms already reflects centrality that is not an artefact of one metric. The sensitivity of the resulting hub set to this threshold was examined by repeating the selection at a stricter three-of-five criterion; the effect of this on hub membership is reported in Supplementary Table S4, and the consensus hub sets derived under both thresholds are provided there in full. Overlapping proteins across cytoHubba methods were identified using venn diagrams with the help of MolBioTools, and the resulting consensus hubs were selected for downstream functional and pathway analyses. To detect highly interconnected functional modules within the network, MCODE (v2.0.3)[48] clustering was performed using the MCODE default parameters, which are reported here explicitly for reproducibility: degree cut-off = 2, node score cut-off = 0.2, K-core = 2 and maximum depth from seed = 100, with haircut enabled, fluff disabled and loops excluded. Clusters were ranked by the MCODE score (cluster density multiplied by the number of nodes in the cluster).

Terminology. Because the interaction networks are assembled from protein–protein interaction data whereas the transcriptomic layer is gene-based, the following terms are used consistently throughout. "Hub protein" denotes a node meeting the consensus centrality criterion defined above within a protein–protein interaction network. "DEG" denotes a gene called differentially expressed in the GSE240226 UVA-versus-control contrast. "Hub gene" is used only where a gene-level identifier is required for downstream gene-centric analyses (functional enrichment), and refers to the gene encoding a hub protein. Where a molecule is described as both a hub and a DEG, this means that the protein met the topological criterion and that its encoding transcript was differentially expressed; it does not imply that protein abundance itself was measured, which it was not.

Integrated HA–AA network construction and hub overlap analysis

To examine coordinated network regulation under ultraviolet stress, hyaluronic acid (HA)– and ascorbic acid (AA)–associated interactomes were merged to generate an integrated HA–AA protein–protein interaction network. Differentially expressed genes and hub proteins identified from the individual HA and AA networks were mapped onto the integrated network to assess overlap and network convergence. Hub overlap analysis was performed by comparing consensus hub sets derived from cytoHubba rankings across the individual and integrated networks. This approach enabled identification of shared and system-specific regulatory nodes reflecting coordinated extracellular matrix and redox network responses to UVA exposure.

Functional enrichment analysis

Differential expression analysis was performed to identify genes whose transcript abundance is directly altered by UVA exposure, and functional enrichment analysis of these differentially expressed genes (DEGs) was conducted via ShinyGo (v0.85.1),[49,50] to determine which biological processes are transcriptionally responsive to ultraviolet stress in skin fibroblasts. This DEG-based enrichment captures the immediate molecular consequences of UVA irradiation at the gene expression level. In parallel, network-based hub enrichment analysis was performed to address a complementary question: which molecular pathways are governed by the most topologically central and regulatory nodes within the integrated hyaluronic acid–ascorbic acid (HA–AA) interaction network under UVA stress. While DEG enrichment reflects the breadth of UVA-induced transcriptional perturbations, hub-based enrichment highlights the core regulatory programs that may exert disproportionate control over network behaviour, HA length–

dependent interactions, and redox-modulated signalling. Together, these layered enrichment strategies enable distinction between global UVA-responsive effects and the key network controllers orchestrating HA–AA–mediated stress adaptation.

Enrichment parameters. Enrichment was computed in ShinyGO v0.85.1 against its bundled human annotation, using the hypergeometric test with Benjamini–Hochberg correction of the false discovery rate and an FDR significance cut-off of 0.05. The statistical background was the default ShinyGO background comprising all annotated human protein-coding genes [AUTHORS: CONFIRM — if a custom background (for example, the 177-protein integrated interactome) was supplied instead, state it here, as the choice of background materially affects the reported FDR values]. The maximum number of returned pathways was set to 20 and the minimum pathway size to 2. Because the hub and DEG gene sets are small (12 and 31 genes respectively), enrichment results are interpreted qualitatively and the absence of a significant term is not treated as evidence of absent biological involvement. Complete enrichment outputs for all gene sets and ontologies, including non-significant terms, are provided in Supplementary Table S5.

In silico ligand–protein interaction assessment

For molecular docking, the structures of target proteins were obtained from the RCSB Protein Data Bank,[51,52,60,61] or predicted using AlphaFold [53], for proteins lacking experimentally resolved structures, and prepared in UCSF ChimeraX (v1.11)[53] by removing crystallographic water molecules and irrelevant heteroatoms, followed by addition of hydrogens, charge assignment, and energy minimization to relieve local geometrical strain prior to docking. Oligosaccharide ligands, including hyaluronic acid fragments (HA4, HA6, and HA8), were constructed and geometry-optimized using the GLYCAM-Web platform.[54] Subsequent docking simulations were performed using Molegro Virtual Docker (v7.0),[55] and predicted docking favourability was evaluated using the MolDock score, Rerank score and hydrogen-bonding energy. These are empirical scoring-function outputs used here to rank predicted structural compatibility; they are not measurements of binding affinity and are not interconvertible with experimentally determined dissociation constants or free energies of binding.

Rationale for HA oligomer selection. HA4, HA6 and HA8 were selected to span the size range over which hyaluronan switches biological behaviour while remaining tractable for rigid-receptor docking. HA4 (a tetrasaccharide) is close to the minimum fragment length reported to occupy the CD44 Link module; HA6 (a hexasaccharide) corresponds to the oligomer length resolved in the CD44 co-crystal structure and is the shortest fragment generally accepted to support stable receptor engagement; and HA8 (an octasaccharide) extends beyond the canonical groove and was included specifically to probe whether increasing chain length reduces predicted compatibility. Longer, physiologically abundant HA polymers were not modelled because their conformational flexibility exceeds what rigid-receptor docking can sample meaningfully. All three oligomers were built as β1→4/β1→3-linked D-glucuronic acid–N-acetyl-D-glucosamine repeats and geometry-optimised on the GLYCAM-Web platform before docking; because each oligomer was docked in a single optimised conformation, the resulting scores should be read as conformation-specific predictions rather than as conformationally averaged estimates.

Docking protocol and ligand preparation. Docking used the MolDock SE search algorithm with the MolDock [GRID] scoring function at an energy grid resolution of 0.30 Å. Candidate binding cavities were detected automatically in Molegro Virtual Docker using the expanded van der Waals cavity-detection algorithm. For CD44 (PDB 1UUH) and LYVE1 (PDB 8OS2) the search space was centred on the experimentally defined Link-module hyaluronan-binding groove; for CLIC1, GSTO1, SLC2A3 and SLC2A14 the search space was centred on the highest-volume detected cavity. The exact search-space definition for each receptor — cavity rank and volume, centre coordinates (x, y, z) and search radius in Å — is reported in Supplementary Table S6 [AUTHORS: INSERT THESE COORDINATES AND RADII FROM THE MVD CAVITY DETECTION LOG]. The following search parameters were applied: number of runs = 5, population size = 50, maximum iterations = 1500, maximum steps = 300, neighbour distance factor = 1.00 and energy threshold = 100.00; poses within an RMSD of 1.00 Å were clustered and only the highest-ranked pose per cluster was retained, yielding the five poses reported per complex. Ligands were prepared at physiological pH, with the glucuronic acid carboxylate groups of the HA oligomers modelled in the deprotonated state and dehydroascorbate modelled in its neutral bicyclic hemiketal form. [AUTHORS: STATE WHETHER THE PROTOCOL WAS VALIDATED BY REDOCKING A CO-CRYSTALLISED LIGAND — the HA hexasaccharide resolved in CD44 structure 1UUH provides a suitable redocking control — AND REPORT THE RESULTING RMSD. If no redocking validation was performed, this must be stated as a limitation.]

Results

Ultraviolet-responsive transcriptional remodelling and topological hub identification in hyaluronic acid and ascorbic acid networks

Protein–protein interaction networks were analysed for curated sets of hyaluronic acid–associated (n = 88) and ascorbic acid–associated (n = 90) human proteins following integration with ultraviolet (UVA) exposure–responsive transcriptomic data. Mapping of UVA-regulated genes onto these interactomes enabled evaluation of transcriptional perturbations within ligand-specific signalling contexts. In the hyaluronic acid interactome, integration of UVA-responsive genes yielded a densely connected network architecture (Figure 2A). 17 HA-associated genes were significantly altered following UVA exposure, comprising 13 downregulated and 4 upregulated genes, indicating a predominantly suppressive transcriptional response. Visualization of these genes within the network revealed that several UVA-responsive nodes occupied central positions within the interactome. Topological analysis identified a subset of highly connected hub proteins (Figure 2B), with multiple UVA-responsive genes intersecting this hub set, suggesting that UVA-induced transcriptional changes preferentially affected functionally central components of the HA network.

Copyright: ©2026 Ghatak et al.

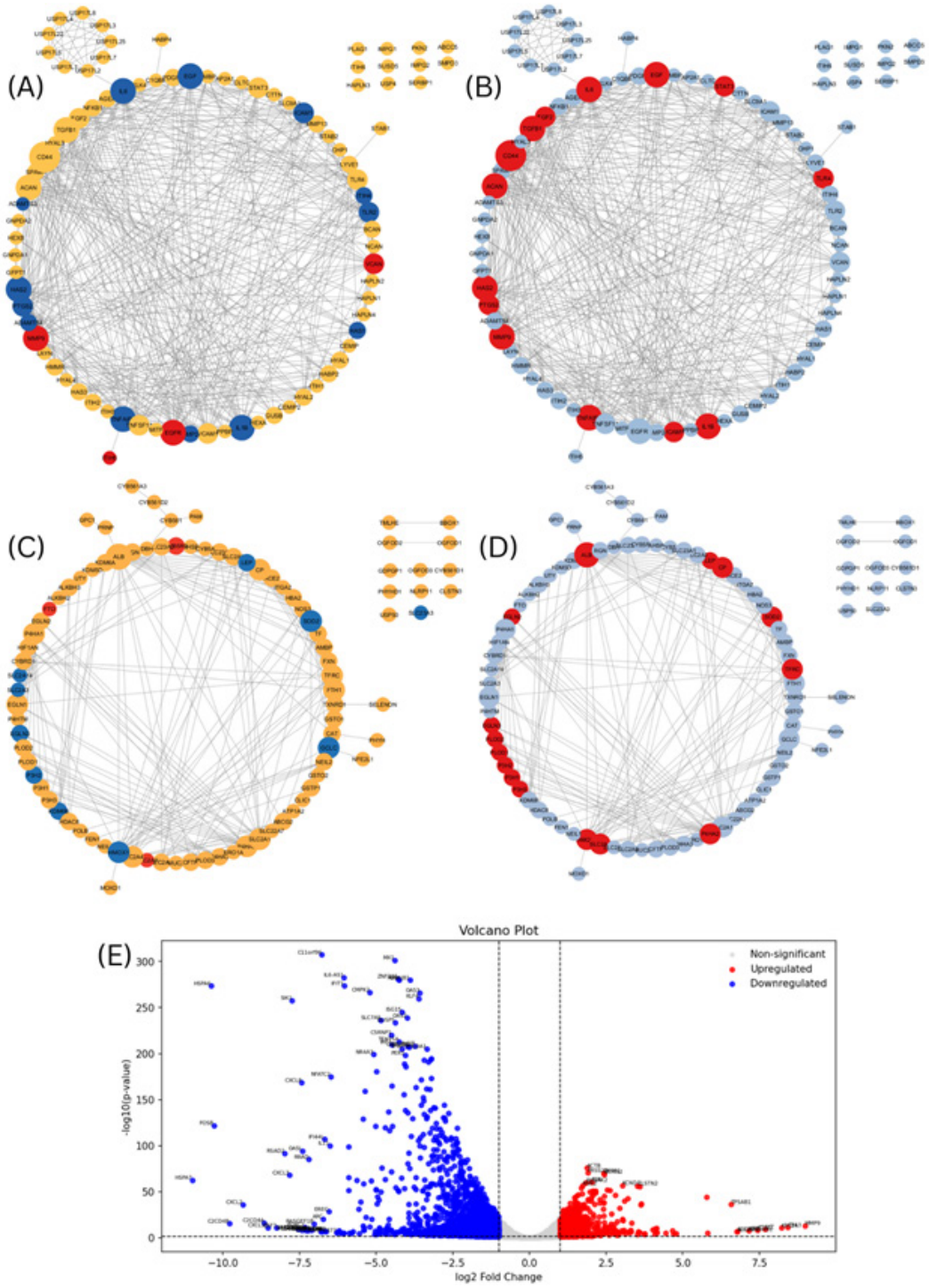

Figure 2 Differential expression mapping and hub identification in hyaluronic acid (HA) and ascorbic acid (AA) interactomes under UVA exposure. (A) DEG-mapped protein–protein interaction (PPI) network of the HA-associated interactome under UVA exposure. Nodes represent HA-associated proteins and edges indicate known or predicted interactions retrieved from STRING. Differentially expressed genes (DEGs) are highlighted, with upregulated genes shown in red and downregulated genes shown in blue, while non-DEG interactors are displayed in grey. (B) Identification of hub proteins within the HA interactome using CytoHubba. Hub proteins are highlighted in red, representing nodes with high topological centrality and potential regulatory importance, whereas non-hub proteins are shown in grey. Node size corresponds to hub status, with enlarged nodes indicating hub proteins. (C) DEG-mapped protein–protein interaction (PPI) network of the AA-associated interactome under UVA exposure. Nodes represent AA-associated proteins and edges indicate known or predicted interactions. Upregulated DEGs are shown in red, downregulated DEGs in blue, and non-DEG interactors in grey. (D) Identification of hub proteins within the AA interactome using CytoHubba, with hub proteins highlighted in red and non-hub interactors shown in grey. Node size reflects hub status, with enlarged nodes denoting hub proteins.(E) Volcano plot illustrating differential gene expression between UVA-exposed and control samples. Significantly upregulated genes are shown in red, significantly downregulated genes in blue, and non-significant genes in grey, based on $\log_2$ fold-change and adjusted p-value thresholds.

Citation: Ghatak K, Rani K. A systems-level computational analysis of UVA-responsive hyaluronic acid and ascorbic acid interactomes and ligand–protein interactions in human skin. *J Bacteriol Mycol Open Access.* 2026;14(3):88–108. DOI: 10.15406/jbmoa.2026.14.00435

A comparable pattern was observed in the ascorbic acid interactome (Figure 2C). 13 AA-associated genes were differentially regulated under UVA exposure, including 10 downregulated and 3 upregulated genes. Hub analysis identified a distinct group of highly connected proteins within the AA network (Figure 2D). UVA-responsive genes were primarily embedded within redox- and transport-associated regions, with selected differentially expressed genes overlapping with topologically central nodes. Comparative assessment of the UVA-integrated HA and AA interactomes revealed both shared and pathway-specific responses to UVA exposure. Although the proportion of differentially expressed genes was limited relative to overall network size, formal statistical testing (Table 2) confirmed that this distribution was non-random in the HA interactome, where DEG nodes showed significantly higher degree, betweenness, closeness, stress and radiality than non-DEG nodes. In the AA interactome, by contrast, no centrality metric differed significantly between DEG and non-DEG nodes, so the apparent localisation of AA DEGs to redox- and transport-associated regions reflects their functional annotation rather than a demonstrable topological bias. Overlap analysis identified common UVA-responsive targets within the HA and AA interactomes, indicating functional convergence between ultraviolet stress responses and hyaluronic acid– and ascorbic acid–associated molecular pathways. A global view of UVA-induced transcriptional changes is shown in the volcano plot (Figure 2E), which illustrates the distribution of differentially expressed genes based on effect size and statistical significance. Taken together, these findings indicate that UVA exposure induces selective transcriptional perturbations within both interactomes, with a statistically supported bias towards topologically central nodes in the HA interactome but not in the AA interactome, and without substantial alteration of overall network structure.

Table 1 Topological parameters of the hyaluronic acid, ascorbic acid and integrated HA–AA interactomes, computed in Cytoscape (NetworkAnalyzer, undirected, self-loops excluded). Expected edge counts and PPI enrichment p-values are STRING outputs and must be transcribed from the STRING network statistics panel for each query

Network	Nodes	Edges	Avg. node degree	Avg. clustering coefficient	Disconnected nodes	Connected components	Largest component	Expected edges (STRING)	PPI enrichment p-value (STRING)
Hyaluronic acid interactome	88	481	10.93	0.570	11	12	77	[AUTHORS: INSERT]	[AUTHORS: INSERT]
Ascorbic acid interactome	90	240	5.33	0.397	8	11	78	[AUTHORS: INSERT]	[AUTHORS: INSERT]
Integrated HA–AA network	177	955	10.79	0.457	16	19	157	[AUTHORS: INSERT]	[AUTHORS: INSERT]

Table 2 Comparison of node centrality between differentially expressed (DEG) and non-differentially expressed (non-DEG) nodes in each network. One-sided Mann–Whitney U test (alternative: DEG > non-DEG) with 10,000-fold label-permutation confirmation; rank-biserial correlation is reported as a distribution-free effect size. Permutation p-values are bounded below by the resolution of the permutation procedure (1/10,001)

Network	Centrality metric	Median (DEG)	Median (non-DEG)	Mann–Whitney U	p (one-sided)	p (permutation)	Rank-biserial *r*
HA (17 DEG vs 71 non-DEG)	Degree	24	7	1025.0	4.1×10^{-6}	$< 1 \times 10^{-4}$	+0.698
	Betweenness	0.0278	0.00056	973.5	3.4×10^{-5}	0.0051	+0.613
	Closeness	0.528	0.396	1042.5	1.7×10^{-6}	$< 1 \times 10^{-4}$	+0.727
	Stress	1336	18	981.5	2.3×10^{-5}	2×10^{-4}	+0.626
	Radiality	0.979	0.966	855.5	1.1×10^{-5}	$< 1 \times 10^{-4}$	+0.677
AA (13 DEG vs 77 non-DEG)	Degree	6	5	617.5	0.090 (n.s.)	0.126	+0.234
	Betweenness	0.0084	0.0048	600.0	0.125 (n.s.)	0.243	+0.199
	Closeness	0.318	0.329	521.0	0.409 (n.s.)	0.575	+0.041
	Stress	298	186	602.5	0.119 (n.s.)	0.229	+0.204
	Radiality	0.904	0.911	433.5	0.432 (n.s.)	0.388	+0.032
Integrated (31 DEG vs 146 non-DEG)	Degree	17	7	3270.5	4.9×10^{-5}	$< 1 \times 10^{-4}$	+0.445
	Betweenness	0.0173	0.0012	3246.0	6.3×10^{-5}	0.0012	+0.434
	Closeness	0.421	0.355	3131.5	4.0×10^{-4}	0.035	+0.384
	Stress	4438	297	3279.0	3.7×10^{-5}	2×10^{-4}	+0.449
	Radiality	0.975	0.967	2674.0	1.0×10^{-3}	0.0082	+0.361

Network architecture and statistical testing of DEG centrality

Topological parameters for all three networks are summarised in Table 1. The HA interactome comprised 88 nodes and 481 edges, with an average node degree of 10.93 and an average clustering coefficient of 0.570; 11 nodes were disconnected and the largest connected component contained 77 proteins. The AA interactome was markedly sparser, comprising 90 nodes and 240 edges, with an average node degree of 5.33 and an average clustering coefficient of 0.397; 8 nodes were disconnected and the largest connected component contained 78 proteins. The integrated HA–AA network comprised 177 nodes and 955 edges, with an average node degree of 10.79 and an average clustering coefficient of 0.457; 16 nodes were

disconnected and the largest connected component contained 157 proteins. The approximately two-fold higher edge density of the HA interactome relative to the AA interactome is the structural basis of the hub asymmetry described below, and is considered further in the Discussion in the context of possible ascertainment bias.

To establish whether UVA-responsive genes preferentially occupy central network positions, five centrality metrics were compared between DEG and non-DEG nodes in each network using the one-sided Mann–Whitney U test with 10,000-fold label-permutation confirmation (Table 2). In the HA interactome, DEG nodes (n = 17) showed significantly higher values than non-DEG nodes (n = 71) for every metric tested, with large effect sizes: median degree 24 versus 7 ($U = 1025.0$, $p = 4.1 \times 10^{-6}$; permutation $p < 1 \times 10^{-4}$; rank-biserial $r = +0.70$) and median stress 1336 versus 18 ($U = 981.5$, $p = 2.3 \times 10^{-5}$; permutation $p = 2 \times 10^{-4}$; $r = +0.63$). The same pattern held in the integrated HA–AA network, where DEG nodes (n = 31) exceeded non-DEG nodes (n = 146) on all five metrics (median degree 17 versus 7; $U = 3270.5$, $p = 4.9 \times 10^{-5}$; permutation $p < 1 \times 10^{-4}$; $r = +0.45$). In the AA interactome, however, no metric reached significance (all $p > 0.05$; median degree 6 versus 5, $U = 617.5$, $p = 0.090$; permutation $p = 0.126$), with effect sizes at or below $r = +0.23$. The claim that UVA preferentially perturbs topologically central nodes is therefore statistically supported for the HA and integrated networks but is not supported for the AA network, and is not asserted for it.

Functional class composition of HA- and AA-associated protein sets

PANTHER protein class analysis revealed both shared and distinct functional compositions between the hyaluronic acid (HA) and ascorbic acid (AA) interactomes (Figure 3A–B). In both networks, metabolic interconversion enzymes, protein-modifying enzymes, and transporters constituted the dominant protein classes, indicating enrichment of enzymatic and transport functions. However, marked differences were observed at the subclass level. In the HA interactome (Figure 3A), metabolic interconversion enzymes were predominantly represented by hydrolases, with comparatively lower contributions from oxidoreductases, ligases, and transferases. This profile was accompanied by enrichment of extracellular matrix glycoproteins and scaffold/adaptor proteins, consistent with structural and matrix-associated functions. Protein-modifying enzymes in the HA network were largely proteases, reflecting matrix remodelling and proteolytic regulation. In contrast, the AA interactome (Figure 3B) displayed a distinct subclass distribution within metabolic interconversion enzymes, characterized by a stronger representation of oxidoreductases alongside hydrolases. Transporter proteins in the AA network were predominantly classified as secondary carrier and primary active transporters, highlighting regulated transport and redox-associated metabolic processes. Protein-modifying enzymes were again dominated by proteases, though with reduced representation of matrix-associated structural classes compared to the HA interactome. Overall, while both interactomes share a common enzymatic framework, HA-associated proteins exhibit a hydrolase- and matrix-centred composition, whereas the AA interactome is comparatively enriched in oxidoreductase and transport-related functions, reflecting pathway-specific functional specialisation.

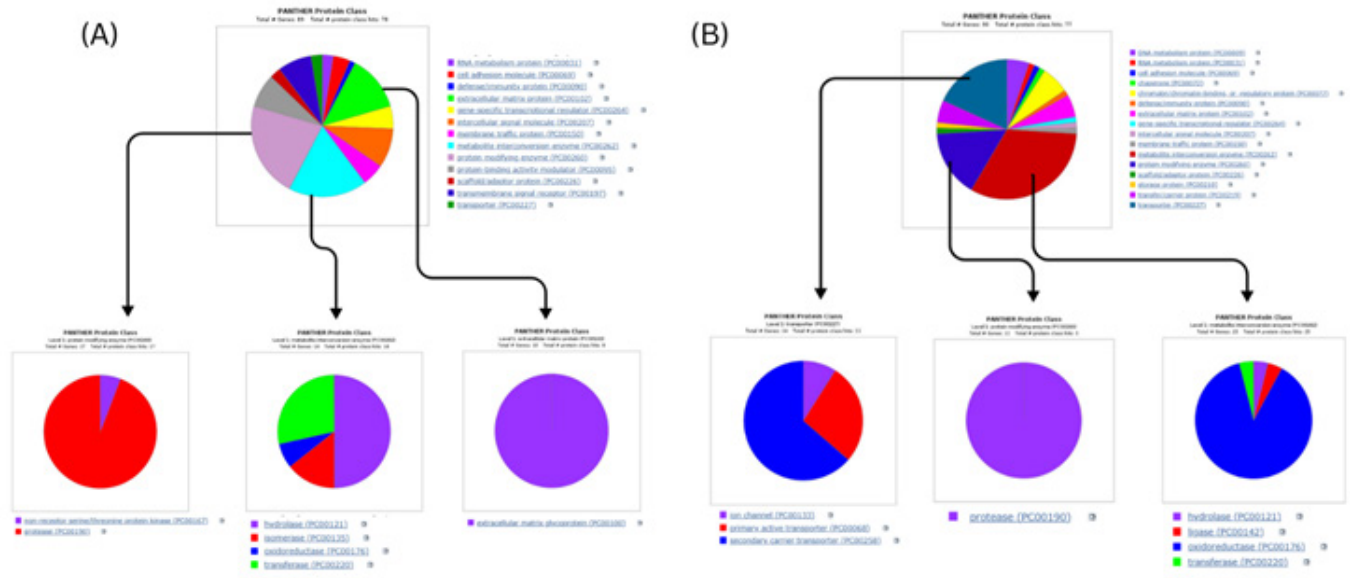

Figure 3 PANTHER protein classification. The overall distribution of protein classes is shown (top), with the three largest protein class categories further expanded to illustrate their subclass composition (bottom panels).(A) HA-associated protein (B) AA-associated protein.

Integrated HA–AA network reveals dominant HA-driven and emergent regulatory hubs

Integration of the hyaluronic acid (HA) and ascorbic acid (AA) interactomes with UVA-responsive transcriptomic data produced a densely connected composite network, reflecting extensive baseline crosstalk between extracellular matrix, inflammatory, metabolic, and redox-associated proteins (Figure 4A). Despite the large size of the integrated interactome, only a limited subset of nodes exhibited transcriptional responsiveness to UVA exposure. Venn analysis demonstrated that 7 upregulated and 24 downregulated genes intersected with the HA–AA interactome [AUTHORS: RECONCILE — the HA network reports 17 DEGs and the AA network 13 DEGs (30 in total), whereas the integrated network reports 31; the additional

gene is CEMIP2, which is annotated "non-UV responsive" in the HA network table but "downregulated" in the integrated network table. Please correct whichever annotation is wrong and update the affected counts consistently], while the majority of UVA-responsive genes lay outside the curated interaction space (Figure 4B), indicating selective rather than global transcriptional perturbation of the HA–AA network.

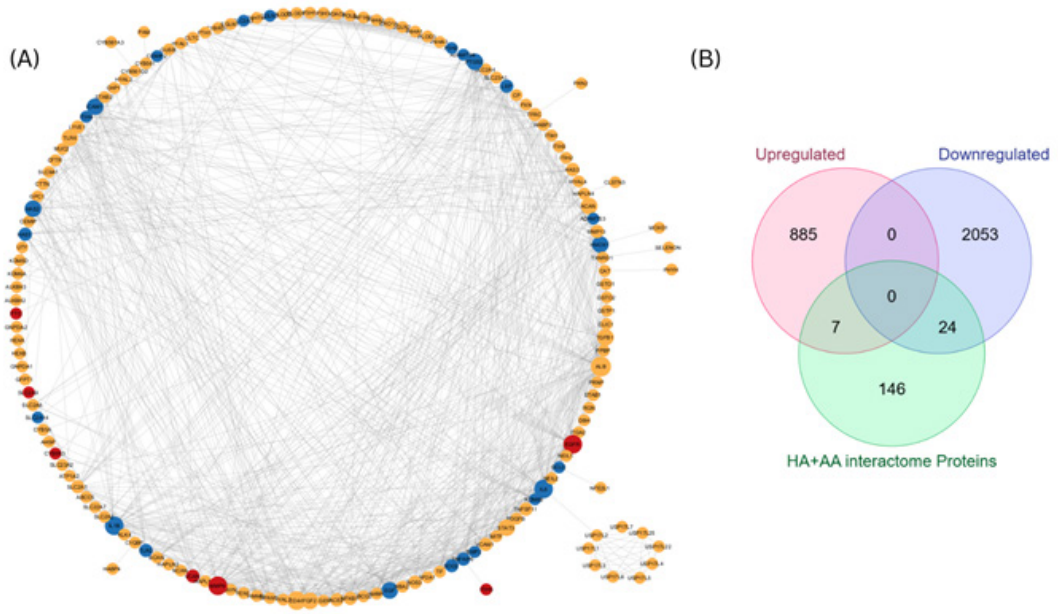

Figure 4 (A) Protein–protein interaction (PPI) network of the UVA-integrated complete hyaluronic acid - ascorbic acid interactome. Nodes represent proteins, and edges indicate known or predicted interactions. Node size reflects degree as determined by MCODE analysis. Coloured nodes are DEGs with upregulated DEGs marked in red and downregulated DEGs marked in blue (B) Venn diagram showing the overlap between upregulated genes, downregulated genes, and proteins within the entire interactome, highlighting a small subset of intersecting genes used for downstream network and functional interpretation analyses.

Mapping of differentially expressed genes (DEGs) onto the integrated network showed that DEGs were positioned within highly connected regions rather than peripheral zones (Figure 4A). This localisation was confirmed statistically (Table 2): DEG nodes in the integrated network had significantly higher degree, betweenness, closeness, stress and radiality than non-DEG nodes (all $p < 0.005$ by one-sided Mann–Whitney U test with permutation confirmation). These data are consistent with UVA exposure perturbing transcriptionally a central rather than a peripheral subset of the HA–AA signalling landscape; they do not, however, establish that UVA acts on those nodes causally or selectively, since transcript-level responsiveness and network centrality are both correlated with the biological prominence that led these proteins to be curated in the first place.

Subsequently, network topological importance was assessed using the cytoHubba plugin. Five complementary centrality algorithms—Maximal Clique Centrality (MCC), Density of Maximum Neighbourhood Component (DMNC), Edge Percolated Component (EPC), Radiality, and Stress centrality— identified distinct but overlapping sets of hub proteins within the HA, AA, and integrated networks. Each method generated a list of the top 10 ranked proteins, summarized in Table 3. Although each algorithm emphasizes different topological features, considerable overlap was observed among the ranked lists. To increase robustness and reduce method-specific bias, proteins appearing in the top 10 rankings of at least two centrality methods were defined as hub proteins. This consensus approach resulted in the identification of 12 hub proteins (Figure 5). Comparative hub overlap analysis revealed asymmetric integration between the HA and AA networks (Table 3). A greater number of hubs were shared between the integrated and HA-specific networks than with the AA-specific network. Among the 12 hubs identified in HA-AA interactome 9 were common with HA-interactome, 1 with AA-interactome and 2 were unique to integrated network illustrated using a Venn diagram (Figure 5C). In the HA-specific network, hub proteins were dominated by inflammatory mediators and extracellular matrix regulators, including IL6, IL1B, CD44, MMP9, TGFB1, PTGS2, VCAM1, and TLR4, consistent with a matrix–inflammatory signalling axis. In contrast, the AA-specific network hubs were involved in redox regulation, collagen modification, and transport processes, such as ALB, SLC2A1, HMOX1, SOD2, TFRC, and EGLN family members, reflecting metabolic buffering and oxidative stress modulation. The integrated HA–AA network retained a substantial proportion of HA-derived hubs while simultaneously introducing novel high-centrality nodes not prominent in the individual networks. Central hubs within the integrated network included IL6, IL1B, CD44, MMP9, TGFB1, STAT3, EGFR, ALB, and SLC2A1, indicating convergence of inflammatory–matrix signalling with metabolic and transport regulation under UVA stress. Notably, a subset of the 12 consensus hubs occupied dual roles as both hub proteins and DEGs: IL6, IL1B and PTGS2 (all downregulated) and MMP9 and EGFR (both upregulated). These five nodes combine topological centrality with transcriptional responsiveness and are therefore proposed as candidate stress-responsive regulatory points within the HA–AA network. The remaining seven consensus hubs — CD44, TGFB1, ALB, STAT3, VCAM1, TLR4 and NFKB1 — were not differentially expressed despite their high centrality. One interpretation of this pattern is that UVA-induced signalling is routed through pre-existing interaction scaffolds without requiring transcriptional induction of every central regulator; this remains a hypothesis, since transcript abundance was the only molecular readout available and post-transcriptional, translational and post-translational regulation of these hubs was not assessed.

Copyright: ©2026 Ghatak et al.

Table 3 Top 10 ranked proteins identified using five CytoHubba centrality algorithms

Methods		DMNC	MCC	EPC	Stress	Radiality
Hyaluronic Acid	1	NFKB1	IL6	CD44	IL6	CD44
	2	AGER	TGFB1	IL6	CD44	IL6
	3	BMP2	FGF2	MMP9	HAS2	ACAN
	4	TNFSF11	CD44	ACAN	USP17L2	IL1B
	5	FGF2	IL1B	IL1B	TNFAIP6	TNFAIP6
	6	VCAM1	PTGS2	EGF	GUSB	TGFB1
	7	TLR4	MMP9	TGFB1	LYVE1	MMP9
	8	PTGS2	TLR4	FGF2	ACAN	EGF
	9	MMP13	VCAM1	TNFAIP6	EGF	HAS2
	10	STAT3	STAT3	PTGS2	EGFR	FGF2
Ascorbic Acid	1	P3H3	P4HA2	ALB	ALB	ALB
	2	HIF1AN	P4HA1	SLC2A1	SLC2A1	SLC2A1
	3	P3H1	PLOD2	TFRC	HMOX1	HMOX1
	4	PLOD1	P3H1	HMOX1	P3H3	TFRC
	5	P3H2	PLOD1	SOD2	DBH	SOD2
	6	PLOD3	P3H2	FTH1	SOD2	LEP
	7	P4HA3	SLC2A1	SLC2A4	GCLC	SLC2A4
	8	EGLN2	EGLN3	CP	CP	ABCG2
	9	PLOD2	EGLN1	LEP	TFRC	NOS3
	10	EGLN3	EGLN2	P4HA2	P4HA2	CP
Integrated Network	1	AGER	IL6	IL6	IL6	IL6
	2	BMP2	IL1B	CD44	SLC2A1	ALB
	3	TNFSF11	MMP9	MMP9	ALB	IL1B
	4	VCAM1	PTGS2	ALB	CD44	MMP9
	5	MMP13	TGFB1	IL1B	EGFR	CD44
	6	NFKB1	ALB	TGFB1	HAS2	EGFR
	7	LEP	STAT3	PTGS2	HMOX1	PTGS2
	8	ITGA2	VCAM1	EGFR	MMP9	TGFB1
	9	FGF2	TLR4	STAT3	IL1B	STAT3
	10	NOS3	NFKB1	TLR4	PTGS2	EGF

Citation: Ghatak K, Rani K. A systems-level computational analysis of UVA-responsive hyaluronic acid and ascorbic acid interactomes and ligand–protein interactions in human skin. *J Bacteriol Mycol Open Access.* 2026;14(3):88–108. DOI: 10.15406/jbmoa.2026.14.00435

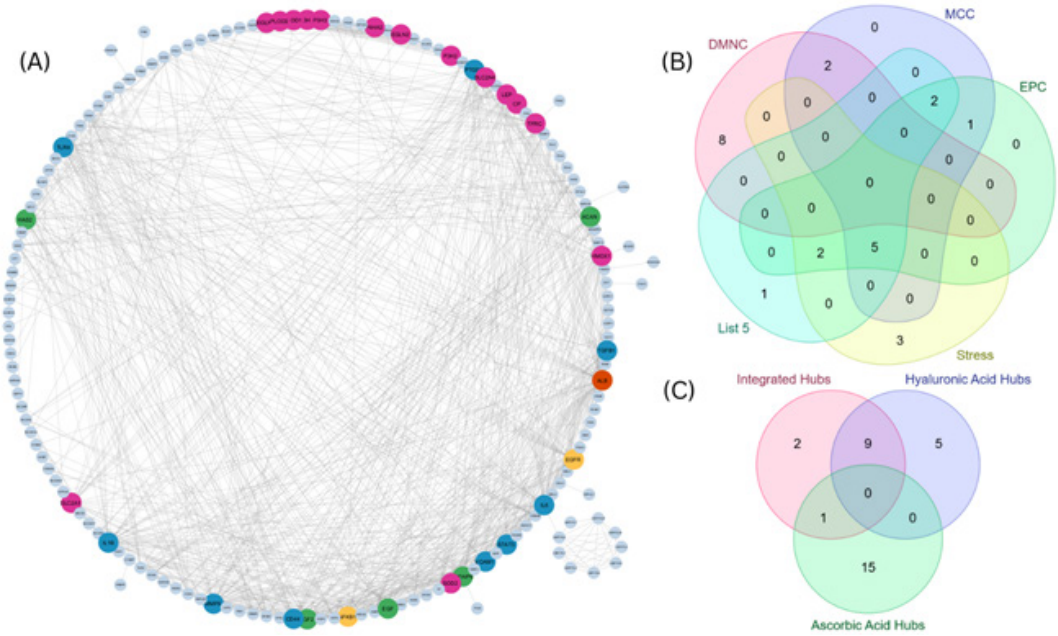

Figure 5 (A) Integrated protein–protein interaction network illustrating hub overlap and emergence between hyaluronic acid (HA) and ascorbic acid (AA) signalling modules under UVA stress. Nodes are coloured according to hub classification: hyaluronic acid-unique hubs (green), ascorbic acid-unique hubs (magenta), hubs shared between the integrated and HA-specific networks (blue), hubs shared between the integrated and AA-specific networks (red), and hubs unique to the integrated network (yellow). Grey nodes represent non-hub interactors. Node size indicates hub status, with larger nodes representing hub proteins and smaller nodes representing non-hub interactors. (B) Venn diagram illustrating the overlap of top-ranked hub genes identified using five complementary CytoHubba centrality algorithms: Maximal Clique Centrality (MCC), Density of Maximum Neighbourhood Component (DMNC), Edge Percolated Component (EPC), Stress, and Radiality. Genes consistently identified across multiple centrality metrics were prioritized as hub proteins for downstream functional interpretation. (C) Venn diagram showing the overlap between hubs identified in individual AA and HA interactomes along with integrated complete interactome according to Cytohubba analysis (Table 3).

Table 3. Top 10 ranked proteins identified using five CytoHubba centrality algorithms*: Density of Maximum Neighbourhood Component (DMNC), Maximal Clique Centrality (MCC), Edge Percolated Component (EPC), Stress, and Radiality, applied independently to the UVA-integrated ascorbic acid interactome, hyaluronic acid interactome as well as HA- and AA- integrated interactome. Proteins appearing among the top ranks across multiple centrality methods were designated as hub genes, reflecting high network connectivity and central positioning. These hub genes were selected for subsequent functional interpretation analyses. The table is arranged as three panels — hyaluronic acid interactome, ascorbic acid interactome and integrated HA–AA interactome — each reporting the five algorithm rankings separately. Applying the consensus criterion (top 10 in at least two algorithms) yields 14 hubs for the HA interactome, 16 for the AA interactome and 12 for the integrated network; consensus hubs are shown in bold within each panel. Overlapping genes are marked in red and genes unique to the HA- and AA- integrated interactome has been marked in green.*

To explore the structural organization of the UVA-integrated HA–AA interactome, MCODE clustering analysis was performed in Cytoscape to identify highly interconnected network modules. This analysis detected 8 significant clusters, 4 of which exhibited MCODE scores greater than 4, indicating strong intra-cluster connectivity (Figure 6). The largest and most densely connected cluster (Fig 6A; MCODE score 21.565) comprises key inflammatory, signalling, and stress-responsive regulators, indicating a dominant regulatory core within the UVA-responsive network. Additional modules include a tightly connected ubiquitin-specific protease cluster (Fig 6B; MCODE score 8.000), an extracellular matrix–associated hyaluronan metabolic cluster (Fig 6C; MCODE score 6.800), and a hypoxia- and collagen-modifying cluster (Fig 6D; MCODE score 4.250). Together, these modules highlight the presence of distinct yet functionally coherent subnetworks within the UVA-integrated interactome, reflecting coordinated regulation of inflammatory signalling, matrix remodelling, redox-associated processes, and hypoxia-linked adaptation in response to UVA exposure.

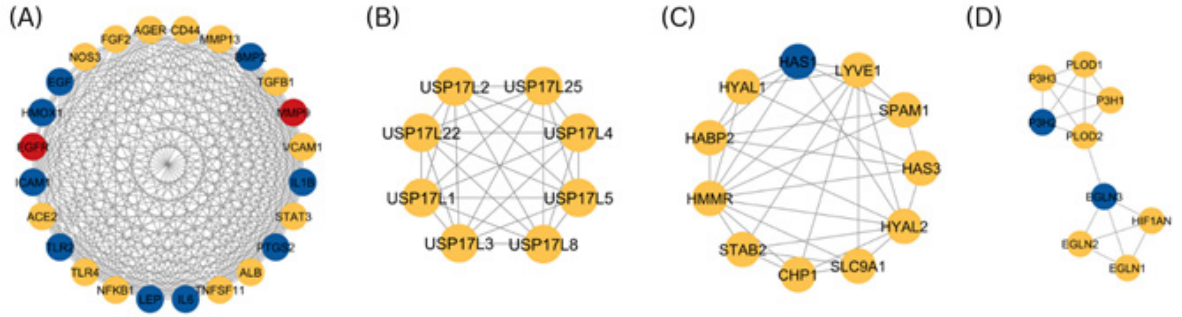

Figure 6 Module detection within the UVA-integrated HA–AA interactome using the MCODE algorithm. Nodes represent proteins and edges indicate protein–protein interactions. Node colour reflects regulation where blue is downregulated and red represents upregulated DEGs. (A) Cluster 1 with a score of 21.565 (24 nodes, 248 edges) (B) Cluster 2 with a score of 8.000 (8 nodes, 28 edges) (C) Cluster 3 with a score of 6.800 (11 nodes, 34 edges) (D) Cluster 4 with a sore of 4.250 (9 nodes, 17 edges).

Functional enrichment of integrated hubs highlights convergent matrix–redox signalling

GO Biological Process (GO_BP) enrichment analysis of hub proteins (Figure 7A) revealed significant involvement of immune- and inflammation-associated processes, including regulation of cell differentiation, cytokine-mediated signalling, lymphocyte and leukocyte activation, inflammatory response, and cellular responses to external and lipid-associated stimuli. These processes are highly relevant to hyaluronan-mediated extracellular signalling and redox-sensitive pathways influenced by ascorbate under UVA-induced stress. KEGG pathway enrichment of hub proteins (Figure 7B) further highlighted convergence on immune and inflammatory signalling cascades, including TNF, IL-17, NF-κB, C-type lectin receptor signalling, and AGE–RAGE pathways, all of which intersect with HA receptor signalling and oxidative stress responses. GO Molecular Function (GO_MF) enrichment of hubs (Figure 7C) showed cytokine receptor binding and signalling receptor binding, underscoring the central role of extracellular ligand–receptor interactions in coordinating the UVA response.

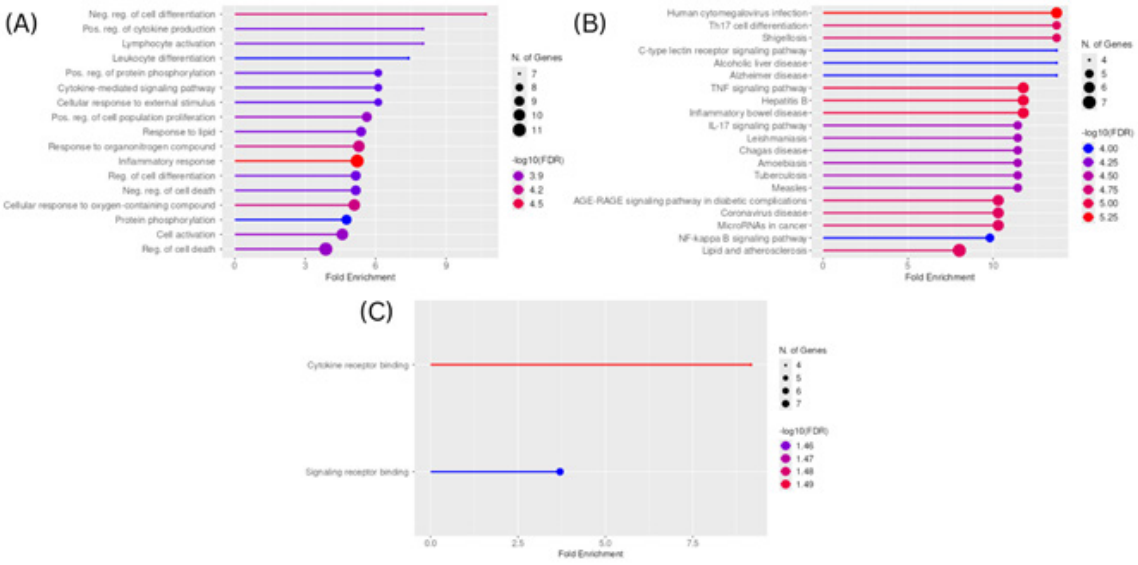

Figure 7 Hub enrichment analysis using ShinyGO. Bubble plots show enrichment results for hub proteins depicting (A) Gene Ontology Biological Process (GO_BP), (B) Kyoto Encyclopedia of Genes and Genomes (KEGG) pathways, and (C) Gene Ontology Molecular Function (GO_MF). Bubble size indicates the number of mapped genes, and colour represents −log10(FDR-adjusted p-value).

In contrast, GO_BP enrichment analysis of UVA-induced differentially expressed genes (Figure 8) identified a narrower functional profile dominated by regulation of cellular catabolic processes, positive regulation of cell migration and locomotion, negative regulation of apoptotic signalling, inflammatory response and regulation of cell population proliferation. These DEG-level terms were, however, only marginally significant (FDR 0.029–0.048) compared with the hub-level terms (FDR as low as 4.9×10^{-5}), and no significant enrichment of GO_MF, KEGG or Cellular Component terms was returned at the DEG level. This difference should not be read as evidence that pathway coordination arises only at the hub level. The DEG set is small (31 genes intersecting the integrated interactome), and a gene set of this size has limited power to reach significance after multiple-testing correction; the absence of significant KEGG

and GO_MF terms is therefore at least as consistent with reduced statistical power and with the narrower annotation coverage of the DEG set as it is with a genuine biological difference. The hub- and DEG-level enrichment profiles are reported here as complementary descriptions of the same network rather than as evidence of distinct levels of regulatory organisation.

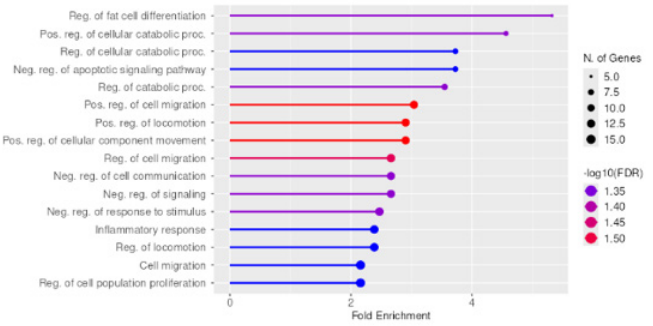

Figure 8 DEG enrichment analysis using ShinyGO. Bubble plots show enrichment results for hub proteins depicting Gene Ontology Biological Process (GO_BP). Bubble size indicates the number of mapped genes, and colour represents −log10(FDR-adjusted p-value).

Network-guided prioritization of receptors and redox proteins for docking analysis

Hyaluronic Acid

The biological impact of HA is mediated by a diverse set of hyaladherins, HA-binding proteins that transduce signals or regulate HA turnover. The selection of the core hyaluronic acid-associated proteins was informed by multiple lines of biological evidence demonstrating functional engagement with low–molecular-weight hyaluronan fragments in prior studies. CD44, the canonical hyaluronan receptor, has long been recognized to mediate HA-dependent cellular responses and has been shown to participate in LMW-HA-driven signalling and receptor complex formation with Toll-like receptors, implicating it in pro-inflammatory responses to HA fragments in diverse cellular contexts [56][57][58]. RHAMM (HMMR) has been documented to bind HA fragments and associate with transmembrane receptors such as CD44, coordinating extracellular HA-dependent signalling relevant to mesenchymal cell behaviour [59]. The lymphatic hyaluronan receptor LYVE-1, a homolog of CD44, has been implicated in HA binding and lymphatic trafficking, and although its affinity is context-dependent, it is widely regarded as a functional HA receptor in lymphatic endothelial biology.[60,61] Pattern-recognition receptors including TLR2 and TLR4 have been repeatedly shown to respond to LMW-HA fragments as danger-associated molecular patterns (DAMPs), eliciting downstream signalling cascades characteristic of HA fragment engagement.[58,62,63] Finally, the receptor for advanced glycation end-products (AGER/RAGE) has been associated with HA fragment-mediated inflammatory signalling in multiple settings, consistent with its role in recognizing endogenous ligands released during tissue injury (reviewed in the context of HA size-dependent effects).[64] Together, these studies provide a literature-anchored basis for including these proteins in the hyaluronic acid interactome and for interrogating their structural compatibility with HA fragment binding in silico. For structure-based interrogation, a deliberate distinction was drawn between proteins with experimentally demonstrated, direct hyaluronan binding and proteins implicated only indirectly in HA-mediated signalling. Only the former were carried into docking. CD44, RHAMM and LYVE-1 have documented direct HA-binding capability supported by structural or mutagenesis evidence; TLR2, TLR4 and AGER/RAGE are implicated in HA fragment-dependent inflammatory signalling but have no reported HA-binding domain or HA-bound structure, and their involvement may be indirect or co-receptor dependent. Accordingly, TLR2, TLR4 and AGER/RAGE were retained in the interactome as signalling interactors but were excluded from docking, and only receptors with both direct binding evidence and structurally resolved extracellular domains were prioritized. CD44 contains a well-characterized HA-binding domain resolved by X-ray crystallography and NMR, which directly engages HA oligosaccharides through a lectin-like Link module and undergoes ligand-induced conformational changes upon binding.[65] In addition, RHAMM has been shown to bind HA via conserved basic B-X_7-B motifs, where mutation of these residues abolishes HA binding, supporting its function as a bona fide HA receptor.[66] LYVE-1, a homolog of CD44 expressed on lymphatic endothelium, also contains a structurally defined HA-binding surface and binds both soluble and immobilized HA, mediating HA-dependent lymphatic interactions.[67] In contrast, pattern-recognition receptors such as TLR2/4 lack documented HA-binding domains and high-resolution binding evidence, and although biologically implicated in HA fragment signalling, they have not been shown to bind HA directly.[68] Furthermore, RAGE, despite its role in inflammatory signalling contexts, has no reported structural HA complex, suggesting its engagement with HA fragments may be indirect or co-receptor dependent. CD44 (PDB ID: 1UUH) and LYVE1 (PDB ID: 8OS2) structures were obtained from the Protein Data Bank. Although RHAMM (HMMR) has been implicated in hyaluronan-mediated signalling, it lacks a well-defined, experimentally resolved ligand-binding pocket and is predominantly characterized by intrinsic disorder and surface-mediated interactions. The available AlphaFold-predicted RHAMM structure has a global mean pLDDT of 77.97, but a global mean is an inadequate description of local structural confidence. Inspection of the per-residue pLDDT profile shows that this average is produced by a long, high-confidence central coiled-coil flankedby extended terminal segments in the very-low-confidence range (pLDDT<05000)0,0 0a0n0d0 0t0h0e0 0b0a0s0i0c0 0B0-0$X_0$7-0B0 0h0y0a0l0u0r0o0n0a0n0-0b0i0n0d0i0ng motifs lie within these poorly resolved regions rather than within a compact, well-packed domain. Cavity-based docking against such regions would not be meaningful. [AUTHORS: INSERT THE DOMAIN-LEVEL pLDDT VALUES — residue ranges with their mean pLDDT — FROM THE AlphaFold DB ENTRY, AND CITE THE ENTRY ACCESSION AND VERSION.] To avoid overinterpretation from structurally uncertain models, RHAMM was therefore excluded from structure-based docking analyses in this study, and focus was placed on CD44 and LYVE1, which possess experimentally resolved structures and established hyaluronan-binding domains.

Ascorbic acid

Proteins associated with dehydroascorbate (DHA) biology were identified using an ontology- and keyword-based curation strategy[69] across UniProt and Gene Ontology databases using the terms “dehydroascorbic acid,” “dehydroascorbate,” “dehydroascorbate transport,” and “dehydroascorbate reductase.” A total of 17 non-redundant proteins were identified, of which seven consistently retrieved proteins (CLIC1, GSTO1, GSTO2, SLC2A14, SLC2A2, SLC2A3, and SLC2A8) were defined as the core ascorbic acid machinery and prioritized for downstream analyses. The selection of proteins for dehydroascorbate (DHA) docking was guided by an integrated systems-level framework combining functional annotation of the ascorbic acid machinery, UVA-responsive transcriptomic alterations, and established biochemical roles in intracellular

ascorbate recycling. From the curated core ascorbic acid interactome (n = 7), functional classification revealed two biologically distinct yet complementary protein categories: (i) membrane-associated dehydroascorbate transporters belonging to the SLC2 family, and (ii) intracellular redox-associated proteins involved in the reduction of DHA back to its biologically active ascorbic acid form. This stratification reflects the canonical two-step model of cellular vitamin C homeostasis, in which extracellular ascorbate is oxidized to DHA, transported into cells, and subsequently reduced to ascorbate to maintain redox balance. Integration of this curated machinery with UVA-responsive transcriptomic data identified SLC2A3 and SLC2A14 as overlapping with downregulated differentially expressed genes under UVA exposure, directly implicating perturbation of DHA transport as a component of UVA-induced redox dysregulation. Both proteins belong to the facilitative glucose transporter family and have been shown to mediate high-affinity transport of DHA via glucose transporter mechanisms, thereby serving as primary gateways for DHA uptake into cells. Their shared functional role, combined with transcriptomic downregulation under UVA stress, provided a strong rationale for prioritizing these transporters as docking targets to evaluate the structural compatibility of DHA engagement under conditions relevant to oxidative stress. To complement the transporter-focused analysis and capture the intracellular arm of the ascorbic acid recycling pathway, representative redox-associated proteins were selected from the opposing functional category. CLIC1 and GSTO1 were chosen based on their established roles in redox regulation and enzymatic reduction of DHA. CLIC1 has been implicated in redox-sensitive signalling and glutathione-dependent electron transfer processes, while GSTO1 is a well-characterized glutathione transferase with documented dehydroascorbate reductase activity. Together, these proteins represent key enzymatically active components responsible for restoring intracellular ascorbate levels following DHA uptake. GSTO2, despite belonging to the same functional class, was excluded from docking analysis due to its close paralogous relationship with GSTO1, thereby avoiding functional redundancy and overrepresentation of a single enzymatic activity.

Molecular docking reveals HA oligomer length–dependent receptor selectivity

Docking of HA oligomers with CD44 and LYVE1

CD44 (PDB ID: 1UUH) and LYVE1 (PDB ID: 8OS2) structures were obtained from the Protein Data Bank. For each protein–HA oligomer-protein complex, five independent docking poses were generated using Molegro Virtual Docker, and predicted docking favourability was systematically evaluated using MolDock score, Rerank score and hydrogen-bond energy (Table 4).

Table 4(A) Docking scores of HA oligomers with CD44. Five docking poses were generated per protein using Molegro Virtual Docker. MolDock score, Rerank score, and hydrogen-bonding energy are reported; more negative values indicate more favourable predicted docking. These scores rank predicted structural compatibility and are not measures of binding affinity.

Oligomer	Pose No.	MolDock Score	Rerank score	HBond
HA4	1	-127.621	-79.3351	-21.5149
	2	-118.622	-74.1438	-18.7455
	3	-116.712	-87.3844	-7.89677
	4	-114.227	-81.7364	-20.9401
	5	-113.41	-74.3513	-17.0617
HA6	1	-109.476	-67.5879	-12.8988
	2	-85.4282	69.0029	-4.833
	3	-74.6351	-23.7399	-10.5795
	4	-71.8397	28.3962	-9.22559
	5	-71.7695	40.6063	-9.22559
HA8	1	476.455	2790.73	-2.7069
	2	582.066	3449.39	3.01166
	3	653.433	3764.74	-12.2787
	4	672.58	4146.71	43.6078
	5	699.028	3875.44	18.8321

Table 4(B) Docking scores of HA oligomers with LYVE1. Five docking poses were generated per protein using Molegro Virtual Docker. MolDock score, Rerank score, and hydrogen-bonding energy are reported; more negative values indicate more favourable predicted docking. These scores rank predicted structural compatibility and are not measures of binding affinity.

Oligomer	Pose No.	MolDock Score	Rerank score	HBond
HA4	1	-126.476	5.331	-29.0693
	2	-116.122	4.45622	-18.181
	3	-107.019	9.91287	-20.4169
	4	-97.3705	18.261	-16.8629
	5	-93.4979	-57.1874	-14.9718
HA6	1	-94.3517	-19.908	-11.7795
	2	-83.4208	41.4501	-11.5174
	3	-74.5833	-2.97515	-13.7491
	4	-70.7964	-8.59161	-1.28946
	5	-69.4622	-11.1697	-16.297
HA8	1	-48.0319	90.3365	-13.1599
	2	-44.8757	21.4274	-13.6839
	3	-44.6472	272.851	-14.0915
	4	-37.6302	157.428	-9.7158
	5	-36.2562	238.308	-19.1309

Showing Pose organizer, Surface cavities, Pose cavities & Pose proteins result of molecular docking interaction of CD44 and HA4

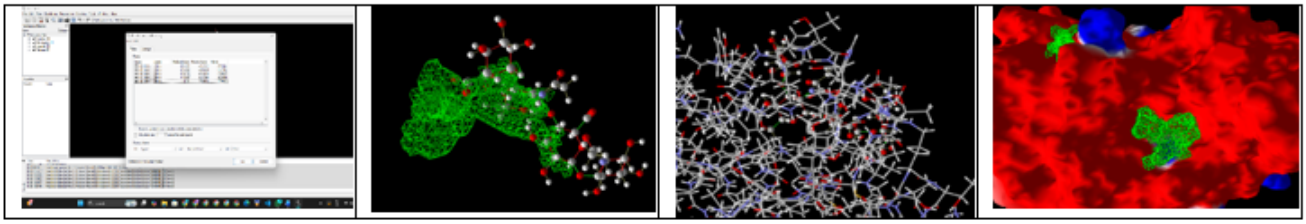

Showing Pose organizer, Surface cavities, Pose cavities & Pose proteins result of molecular docking interaction of CD44 and HA6

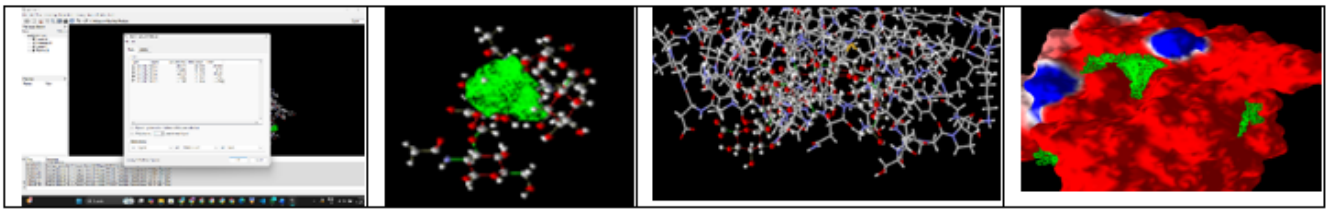

Showing Pose organizer, Surface cavities, Pose cavities & Pose proteins result of molecular docking interaction of CD44 and HA8

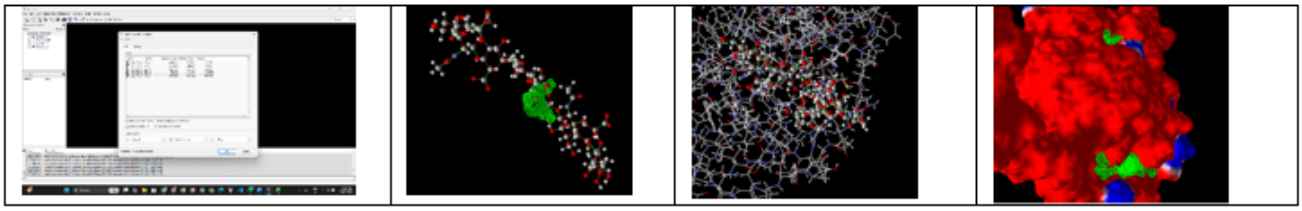

Showing Pose organizer, Surface cavities, Pose cavities & Pose proteins result of molecular docking interaction of LYVE1 and HA4

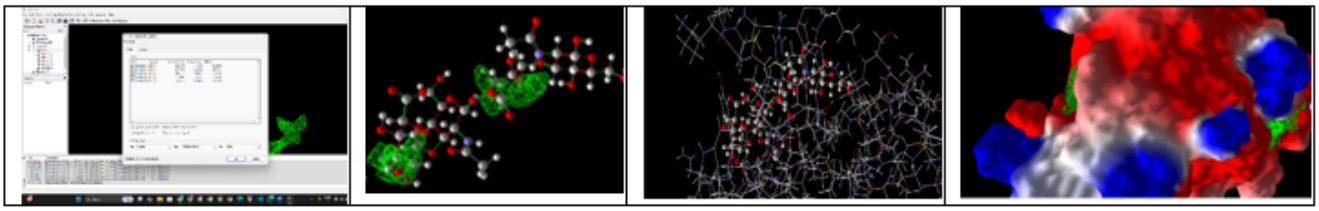

Showing Pose organizer, Surface cavities, Pose cavities & Pose proteins result of molecular docking interaction of LYVE1 and HA6

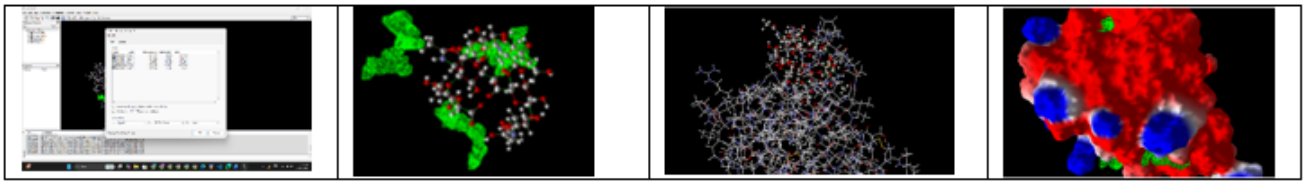

Showing Pose organizer, Surface cavities, Pose cavities & Pose proteins result of molecular docking interaction of LYVE1 and HA8

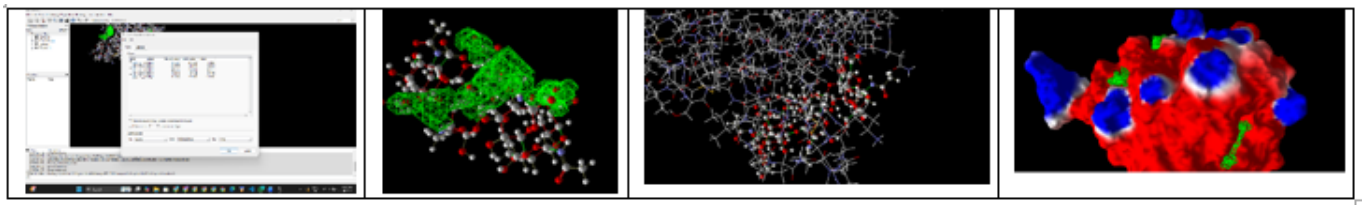

As summarized in Table 4, distinct oligomer length–dependent docking patterns were observed for CD44 and LYVE1. For CD44, shorter hyaluronan oligomers (HA4 and HA6) exhibited consistently favourable interactions, with all five poses yielding negative MolDock scores. HA4 showed the strongest overall binding to CD44, with MolDock scores ranging from −127.62 to −113.41 and substantial predicted hydrogen-bond contributions, consistent with accommodation within the hyaluronan-binding groove. HA6 retained favourable binding in its top-ranked pose (−109.48), although a gradual reduction in binding favourability was evident across subsequent

poses. In contrast, CD44 docking with HA8 resulted in uniformly unfavourable energetics, with all poses displaying strongly positive MolDock and Rerank scores, indicating a loss of productive binding. One possible explanation is steric: HA8 may exceed the spatial constraints of the CD44 hyaluronan-binding groove, producing only partial pocket occupancy and unfavourable scores. This interpretation is a hypothesis rather than a demonstrated structural result. Strongly positive MolDock and Rerank values of the magnitude observed here (MolDock +476 to +699; Rerank +2791 to +4147) indicate severe steric clash in the docked poses and mark the docking run as having failed to find a productive pose; they cannot by themselves be read as evidence that CD44 biologically excludes longer HA fragments. Distinguishing genuine steric exclusion from a failure of the search or scoring procedure would require molecular dynamics simulation, an independent docking engine, or experimental binding measurement. In comparison, LYVE1 demonstrated favourable interactions across all tested hyaluronan oligomers, albeit with a progressive reduction in binding strength with increasing oligomer length. HA4 showed the most favourable binding to LYVE1, with MolDock scores ranging from −126.48 to −93.50 and strong hydrogen-bond contributions across poses. HA6 maintained moderately favourable binding energies (−94.35 to −69.46), while HA8 continued to exhibit negative MolDock scores (−48.03 to −36.26), indicating retained, though weaker, interaction. Collectively, these results predict receptor-specific differences in compatibility with hyaluronan chain length, with CD44 scoring favourably only for the shorter oligomers and LYVE1 retaining favourable scores across all oligomer sizes tested. Because these are docking predictions obtained against single, static receptor conformations, they should be regarded as generating a testable hypothesis of length-dependent receptor discrimination, not as establishing receptor selectivity or physiological permissiveness.

Docking of DHA with redox-associated hub proteins

SLC2A3 (PDB ID: 4ZW9),[70,71] CLIC1 (PDB ID: 7F8R)[72,73] and GSTO1(PDB ID: 3VLN)[74,75] structures were retrieved from Protein Data Bank and SLC2A14, for which no experimental structure is available, was taken from the AlphaFold Protein Structure Database with a global mean pLDDT of 89.81 [AUTHORS: INSERT THE AlphaFold DB ACCESSION (AF-Q8TDB8-F1 OR AS APPLICABLE), THE MODEL VERSION, AND THE MEAN pLDDT FOR THE TRANSMEMBRANE REGION USED FOR DOCKING RATHER THAN THE WHOLE-CHAIN AVERAGE]. Membrane topology was assessed to confirm that the docking cavity lay within the transmembrane channel rather than in a peripheral loop region. For each protein–dehydroascorbate (DHA) complex, five independent docking poses were generated using Molegro Virtual Docker, and predicted docking favourability was evaluated using MolDock score, Rerank score and hydrogen-bond energy (Table 5). The conformational state of each transporter structure is an essential caveat for these results: SLC2A3 (PDB 4ZW9) was resolved in a single conformational state, and the AlphaFold model of SLC2A14 likewise represents one static conformation. Facilitative glucose transporters operate by alternating-access cycling between outward-open, occluded and inward-open states, so docking against a single conformation sample only one point in that cycle and cannot represent substrate recognition or transport competence. [AUTHORS: STATE EXPLICITLY WHICH CONFORMATIONAL STATE 4ZW9 REPRESENTS AND WHICH STATE THE SLC2A14 MODEL CORRESPONDS TO.]

Table 5 Docking scores of dehydroascorbate (DHA) with selected proteins. Five docking poses were generated per protein using Molegro Virtual Docker. MolDock score, Rerank score, and hydrogen-bonding energy are reported; more negative values indicate more favourable predicted docking. These scores rank predicted structural compatibility and are not measures of binding affinity or transport activity.

Protein	Pose No.	Mol Dock Score	Rerank score	H Bond
CLIC1	1	-71.4711	-66.6065	-14.0658
	2	-65.9842	-60.5129	-10.5406
	3	-65.6088	-61.1795	-9.77765
	4	-62.0462	-45.8985	-13.4702
	5	-61.9645	-58.2354	-6.80286
GSTO1	1	-60.481	-54.3983	-9.93391
	2	-57.0229	-52.7768	-9.9405
	3	-55.4405	-46.0061	-4.56441
	4	-55.3077	-50.1693	-7.44492
	5	-53.5787	-50.9831	-4.8086
SLC2A3	1	-81.0941	-74.5449	-19.9935
	2	-77.6189	-72.6529	-15.1471
	3	-74.481	-66.2209	-8.53078
	4	-73.5351	-66.8174	-7.18573
	5	-71.5477	-67.468	-19.5111
SLC2A14	1	-68.9419	-62.1055	-16.7331
	2	-68.1942	-60.3081	-13.4215
	3	-66.1586	-59.6144	-9.09128
	4	-64.4171	-60.6525	-15.9531
	5	-59.6678	-57.3542	-9.03227

Showing Pose organizer, Surface cavities, Pose cavities & Pose proteins result of molecular docking interaction of CLIC1 and DHA

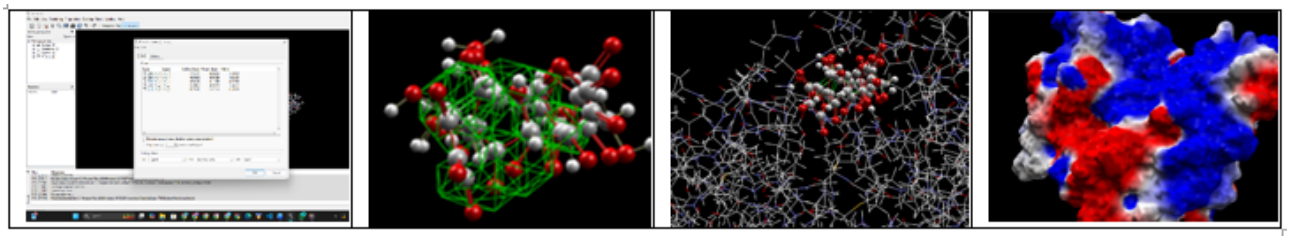

Showing Pose organizer, Surface cavities, Pose cavities & Pose proteins result of molecular docking interaction of GSTO1 and DHA

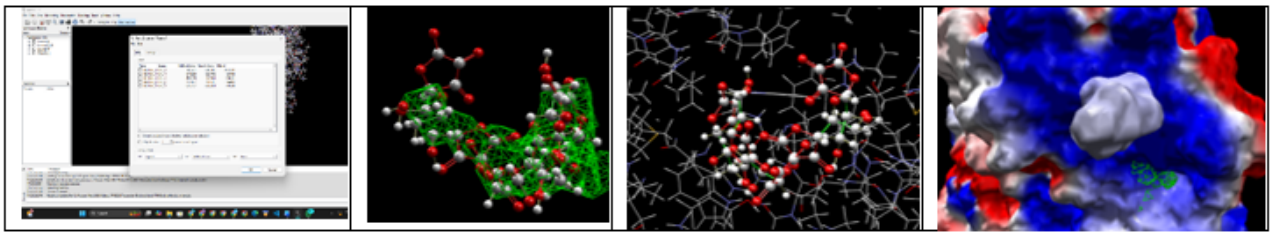

Showing Pose organizer, Surface cavities, Pose cavities & Pose proteins result of molecular docking interaction of SLC2A3 and DHA

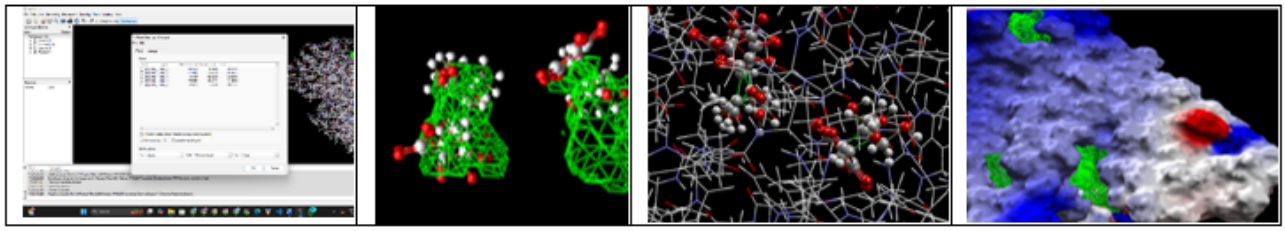

Showing Pose organizer, Surface cavities, Pose cavities & Pose proteins result of molecular docking interaction of SLC2A14 and DHA

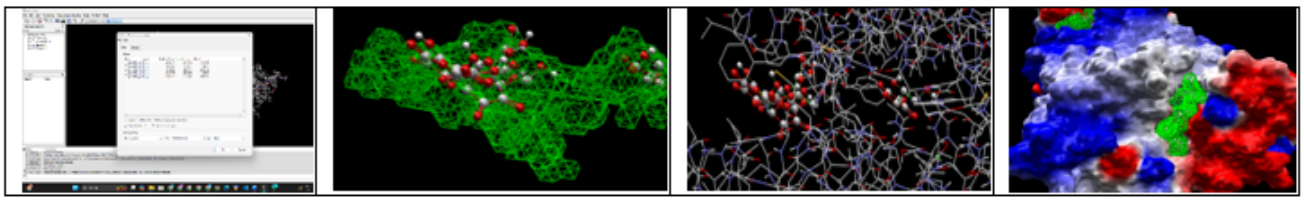

As summarized in Table 5, DHA exhibited energetically favourable predicted docking across all tested proteins, as reflected by consistently negative MolDock scores. Among the redox-associated proteins, CLIC1 displayed the strongest DHA binding, with the top-ranked pose showing a MolDock score of −71.47 and a substantial hydrogen-bonding contribution (−14.07). GSTO1 also returned consistently favourable predicted docking, with the best pose yielding a MolDock score of −60.48 and a hydrogen-bond energy of −9.93. Neither CLIC1 nor GSTO1 was a consensus hub or a DEG in this study; both were selected on the basis of their annotated dehydroascorbate reductase activity, and their docking results should be read in that functional context rather than as network-level findings. The transporter proteins SLC2A3 and SLC2A14 showed comparatively stronger docking scores, particularly SLC2A3, which exhibited the most favourable MolDock score among all proteins tested (−81.09). Docking results for the membrane transporters require particular caution and are not evidence of transport activity. The consistency of favourable scores across multiple poses indicates only that the modelled cavity can sterically and electrostatically accommodate DHA in the single conformational state examined. Because facilitative transporters translocate substrate through a cycle of large conformational changes, static docking of this kind cannot demonstrate substrate recognition, translocation or transport competence, and the results are reported here solely as structural compatibility consistent with the previously established role of these transporters in dehydroascorbate uptake.

Discussion

UVA exposure did not produce widespread transcriptional disruption across either the hyaluronic acid (HA) or ascorbic acid (AA) interaction networks. Instead, transcriptional changes were selective and spatially constrained within the network, with stress-responsive genes showing a clear tendency to occupy highly connected, central positions. Notably, this occurred without substantial alteration of overall network topology. Statistical testing of centrality distributions (Table 2) supports the interpretation that UVA-associated transcriptional change is concentrated at central rather than peripheral positions in the HA and integrated networks, while overall topology is preserved. We emphasise that this is an association observed in a single transcriptomic contrast and not a demonstration that UVA acts selectively on those nodes. The study results show that different types of regulatory systems display different responses to UVA stress through their various extracellular and intracellular frameworks. HA-associated networks dominated the integrated HA–

AA interactome and retained most of the consensus hub proteins (9 of 12 integrated hubs were shared with the HA-specific network, against 1 with the AA-specific network). An important caveat applies to this observation. The curated HA and AA input lists were assembled by keyword-driven database mining, and hyaluronan biology- particularly CD44-dependent inflammatory signalling — is substantially better represented in curated interaction databases than ascorbate redox biology. The HA interactome accordingly entered the analysis roughly twice as densely connected as the AA interactome (481 versus 240 edges for comparable node counts; Table 1). Hub dominance by HA-associated proteins may therefore partly reflect ascertainment and database-selection bias in the input lists rather than an intrinsic property of the underlying biology, and the description of HA signalling as a "structural backbone" should be read with that limitation in mind. Given the extensive connectivity and matrix-centred organization of these networks, we propose — as a biological model to be tested rather than as a demonstrated mechanism — that HA-associated signalling may act as an architectural buffer, maintaining interaction integrity while coordinating inflammatory and extracellular matrix remodelling responses. In contrast, AA-associated networks contributed fewer retained hubs and were enriched primarily for oxidoreductases and transport-related proteins, pointing toward a more modulatory role centred on redox regulation and intracellular metabolic control. This apparent division of roles leads us to hypothesise that stress is not distributed evenly across biological compartments but is instead partitioned between structural stabilisation and functional modulation. This remains a proposed model: the present analysis establishes a difference in network composition and connectivity between the two arms, not a difference in their functional roles under stress, which would require perturbation experiments to demonstrate. The integrated network contained multiple genes that functioned as both hub connectors and differentially expressed genes. These genes — IL6, IL1B and PTGS2 (downregulated) and MMP9 and EGFR (upregulated)- are proposed as candidate regulatory bottlenecks through which UVA-associated signalling may be routed within HA–AA pathways. At the same time, a subset of highly central proteins (CD44, TGFB1, ALB, STAT3, VCAM1, TLR4 and NFKB1) remained transcriptionally stable despite their topological importance. This indicates that UVA-driven responses are routed through existing signalling scaffolds rather than requiring transcriptional induction of all central regulators, highlighting the importance of pre-established network architecture in shaping stress responses. Functional enrichment analyses further reinforce this network-centric view. While differentially expressed genes alone showed limited functional enrichment, hub-centric analysis revealed coherent programs related to inflammatory signalling, extracellular matrix organization, and redox homeostasis. This discrepancy suggests that coordinated biological responses under UVA stress emerge at the level of network organization rather than from isolated transcript-level changes. Directional expression patterns among hub-associated genes are compatible with concurrent activation of matrix remodelling alongside altered inflammatory and redox-associated transcription. We note, however, that the principal inflammatory hubs IL6, IL1B and PTGS2 were downregulated rather than upregulated in this dataset at the 3 h post-irradiation timepoint sampled, so the data do not support a simple description of a shift toward a pro-inflammatory state; the directionality observed here may instead reflect the early timepoint of the contrast, and later timepoints would be required to characterise the trajectory of the response. From a translational standpoint, this study does not aim to define definitive clinical biomarkers. Instead, it provides a comparative, hypothesis-generating framework that integrates differential expression analysis, interactome topology, and structure-based interaction feasibility to prioritize candidate predictive markers along HA- and AA-regulatory axes. By distinguishing between ECM-driven HA signalling and redox-regulated AA metabolism, this approach may help generate hypotheses about which molecular pathways predominate under particular dermatological conditions. Any extension of these hypotheses to oncogenic settings is speculative: no cancer tissue, cancer cell line or tumour transcriptomic data were analysed in this study. This prioritisation rests on a single transcriptomic dataset (GSE240226) comprising one UVA contrast with three biological replicates per group, and it has not been validated against independent datasets. Cross-dataset replication, ideally spanning multiple UVA doses, timepoints and cell types, is a necessary next step before any of these candidates can be regarded as robust.

Limitations

Several limitations constrain the interpretation of this work. First, the study is entirely computational; no experimental validation of any predicted interaction, hub assignment or expression change was performed, and all findings are hypothesis-generating. Second, the transcriptomic layer rests on a single GEO series (GSE240226) with one UVA dose (2 J/cm²), one post-irradiation timepoint (3 h), one cell type (primary human dermal fibroblasts) and three biological replicates per group; the response of keratinocytes, melanocytes, immune and lymphatic endothelial cells, all of which contribute to HA and ascorbate biology in intact skin, is not represented, and no conclusions about chronic or repeated UVA exposure can be drawn from a single acute contrast. Third, the curated protein lists were assembled by keyword-based database mining and therefore inherit the annotation bias of the source databases, which favour well-studied hyaluronan biology over ascorbate redox biology; this bias plausibly contributes to the HA dominance reported here. Fourth, the interaction networks are restricted to experimentally supported and curated STRING interactions, so genuine but uncharacterised interactions are necessarily absent, and network centrality partly reflects research attention rather than biological importance alone. Fifth, all docking was performed against single, static receptor conformations with rigid receptors; this is a particularly severe limitation for the SLC2A transporters, which function through alternating-access conformational cycling, and it also means that HA oligomer scores are conformation-specific. Docking scores are empirical ranking functions and are not equivalent to binding free energies. Sixth, no molecular dynamics simulation, redocking validation or independent scoring function was used to corroborate the docking predictions. Finally, protein abundance was never measured: the transcriptomic layer reports mRNA, and transcript-level stability of a hub does not exclude regulation of that hub at the protein level.

Conclusion

This study integrated curated hyaluronic acid– and ascorbic acid–associated protein interaction networks with UVA-responsive transcriptomic data and structure-based docking. Four findings are directly supported by the analyses presented. First, curated network integration produced an HA interactome of 88 proteins and 481 interactions, an AA interactome of 90 proteins and 240 interactions, and an integrated network of 177 proteins and 955 interactions. Second, UVA-associated differential expression mapped selectively rather than globally onto these networks, and DEG nodes showed significantly higher centrality than non-DEG nodes in the HA and integrated networks (Mann–Whitney U with permutation confirmation, $p < 0.005$ across five centrality metrics) but not in the AA network. Third, consensus hub analysis across five centrality algorithms identified 12 hubs in the integrated network, 9 of which were shared with the

HA-specific network and 1 with the AA-specific network, indicating an asymmetric contribution of the two arms; five of these hubs (IL6, IL1B, PTGS2, MMP9, EGFR) were also differentially expressed. Fourth, docking predicted oligomer length–dependent differences in HA receptor compatibility, with CD44 scoring favourably only for HA4 and HA6 while LYVE1 scored favourably across HA4, HA6 and HA8, and predicted favourable accommodation of dehydroascorbate by CLIC1, GSTO1, SLC2A3 and SLC2A14. On the basis of these observations, we propose, as a model for experimental testing rather than as an established mechanism, that HA-centred extracellular networks and AA-associated intracellular networks may contribute asymmetrically to the cutaneous UVA response, the former through densely connected matrix and inflammatory signalling and the latter through redox and transport processes. We stress that the asymmetry demonstrated here is one of network composition and connectivity, and that it may in part reflect the differing database coverage of the two fields rather than a difference in biological organisation. Chronic UV exposure is a recognised driver of skin ageing and inflammation, and the molecular determinants governing the transition from adaptive stress responses to pathological remodelling remain poorly defined. The candidate nodes identified here may be of interest in that context, but the present study analysed an acute UVA contrast in cultured dermal fibroblasts and examined no disease tissue, no chronic exposure model and no clinical outcome. Implications for carcinogenesis, disease progression, therapeutic resistance or treatment-associated toxicity are therefore not tested by these data and are not claimed. Importantly, the framework does not seek to define definitive biomarkers, but rather to prioritize pathway-level vulnerabilities that may differ across disease contexts and patient populations. Looking forward, this computational framework can be extended to other environmental stressors, tissue types, and oncogenic settings where extracellular matrix dynamics and redox balance play central roles. Integration with longitudinal transcriptomic data, patient-derived datasets, and experimental perturbation studies will be essential to test the predictive value of the identified network features and to refine their clinical relevance. In summary, coupling network topology with structure-based interaction modelling provides a practical way to generate testable hypotheses about molecular stress responses. Every result reported here is computational, and each of the candidate nodes and interactions identified requires experimental validation before any biological or therapeutic significance can be attributed to it.

Declarations

Ethics approval and consent to participate: Not applicable. This study is entirely computational and analysed only previously published, publicly archived, fully anonymised datasets and publicly available protein structures. No human participants, human tissue, identifiable human data or animals were involved, and no new experimental data were generated.

Consent for publication: Not applicable. The manuscript contains no data, images or details relating to any individual person.

Clinical trial registration: Not applicable. This study is not a clinical trial and involved no prospective assignment of human participants to any intervention.

Funding: [AUTHORS: STATE ALL FUNDING SOURCES WITH GRANT NUMBERS, OR STATE "This research received no specific grant from any funding agency in the public, commercial or not-for-profit sectors."]

Authors' contributions: [AUTHORS: INSERT CONTRIBUTIONS PER AUTHOR USING Credit ROLES — conceptualisation, methodology, formal analysis, investigation, data curation, writing – original draft, writing – review and editing, visualisation, supervision. All authors read and approved the final manuscript.]

Availability of data and materials

All data analysed in this study are publicly available and no restricted or author-held datasets were used. The transcriptomic dataset is available from the NCBI Gene Expression Omnibus under accession GSE240226 (https://www.ncbi.nlm.nih.gov/geo/query/acc.cgi?acc=GSE240226), platform GPL24676; the samples used in the present analysis were GSM7688465–GSM7688467 (untreated control) and GSM7688468–GSM7688470 (UVA). Protein annotations were obtained from UniProtKB (https://www.uniprot.org), chemical–protein associations from STITCH v5.0 (http://stitch.embl.de), protein–protein interactions from STRING v12 (https://string-db.org), and protein family classifications from PANTHER v19.0 (https://www.pantherdb.org). Protein structures were obtained from the RCSB Protein Data Bank under accessions 1UUH (CD44), 8OS2 (LYVE1), 4ZW9 (SLC2A3), 7F8R (CLIC1) and 3VLN (GSTO1), and the SLC2A14 model from the AlphaFold Protein Structure Database (https://alphafold.ebi.ac.uk). Functional enrichment was performed with ShinyGO v0.85.1 (http://bioinformatics.sdstate.edu/go/). Analyses were carried out in Cytoscape v3.10.3 with the cytoHubba and MCODE plugins, and in Molegro Virtual Docker v7.0. The complete curated protein lists, DEG list with $\log_2$ fold-changes and adjusted p-values, network statistics, hub rankings for all five centrality algorithms, full enrichment outputs, docking parameters and complete docking outputs are provided as Supplementary Tables S1–S6. The Cytoscape session files, the analysis script used for the centrality statistics and the docking result files are available at [AUTHORS: DEPOSIT THESE IN A PUBLIC REPOSITORY SUCH AS Zenodo, figshare OR OSF AND INSERT THE DOI HERE — the phrase "available from the corresponding author on reasonable request" is not sufficient for this manuscript].

Supplementary material

Supplementary Table S1. Complete curated hyaluronic acid–associated (n = 88) and ascorbic acid–associated (n = 90) human protein lists, with UniProt accessions, gene symbols, protein names, source database (UniProtKB and/or STITCH) and STITCH confidence scores where applicable.

Supplementary Table S2. Complete list of differentially expressed genes from the GSE240226 UVA-versus-control contrast, with $\log_2$ fold-change, nominal p-value and Benjamini–Hochberg adjusted p-value, and an indicator of membership of the HA, AA and integrated interactomes.

Supplementary Table S3. Complete topological statistics for the HA, AA and integrated HA–AA networks, including per-node degree, betweenness, closeness, stress, radiality and clustering coefficient, together with the STRING network summary statistics for each query.

Supplementary Table S4. Full top-10 hub rankings for all five cytoHubba centrality algorithms (MCC, DMNC, EPC, Stress, Radiality) in each of the three networks, with the consensus hub sets derived under both the two-of-five and the stricter three-of-five agreement thresholds.

Supplementary Table S5. Complete ShinyGO enrichment results for the hub and DEG gene sets across GO Biological Process, GO Molecular Function, GO Cellular Component and KEGG, including non-significant terms, with fold enrichment, gene counts, pathway sizes and FDR values.

Supplementary Table S6. Complete molecular docking parameters and outputs, including per-receptor cavity coordinates, search radii, search parameters, ligand preparation details and all generated poses with MolDock score, Rerank score and hydrogen-bond energy.

Acknowledgements

We would like to express my cordial appreciation to Amity University Uttar Pradesh, Noida (INDIA).

Conflicts of interest

The authors declare that there are no conflicts of interest.

References

1. Zanchetta C, Scandolera A, Reynaud R. Hyaluronic acid in topical applications: the various forms and biological effects of a hero molecule in the cosmetics industry. *Biomolecules* 2025;15:1656.
2. Palenčárová K, Köszagová R, Nahálka J. Hyaluronic acid and its synthases—current knowledge. *Int J Mol Sci*. 2025;26:7028.
3. Juhaščik M, Kováčik A, Huerta-Ángeles G. Recent advances of hyaluronan for skin delivery: from structure to fabrication strategies and applications. *Polymers (Basel)*. 2022;14:4833.
4. Šínová R, Pavlík V, Ondrej M. Hyaluronan: A key player or just a bystander in skin photoaging? *Exp Dermatol.* 2022;31:442–458.
5. Žádníková P, Šínová R, Pavlík V. The degradation of hyaluronan in the skin. *Biomolecules*. 2022;12:251.
6. Marinho A, Nunes C, Reis S. Hyaluronic acid: a key ingredient in the therapy of inflammation. *Biomolecules*. 2021;11:1518.
7. Karabat MU, Tuncer MC. Effects of hyaluronic acid on skin at the cellular level: a systematic review. *Rev Assoc Med Bras*. 2025;71:e20250208.
8. Papakonstantinou E, Roth M, Karakiulakis G. Hyaluronic acid: a key molecule in skin aging. *Dermatoendocrinol*. 2012;4:253.
9. Wang J, Martinotti S, Li H. *Role of vitamin C in skin diseases*. 2018..
10. Pullar JM, Carr AC, Vissers MCM. The roles of vitamin C in skin health. 2017;9(8):866.
11. Wei M, He X, Liu N. Role of reactive oxygen species in ultraviolet-induced photodamage of the skin. *Cell Div*. 2024;19:1.
12. Vitamin C and Skin Health | Linus Pauling Institute | Oregon State University, 2026.
13. Kawashima S, Funakoshi T, Sato Y. Protective effect of pre-and post-vitamin C treatments on UVB-irradiation-induced skin damage. *Scientific reports*. 2018;8:16199.
14. Gęgotek A, Bielawska K, Biernacki M. Comparison of protective effect of ascorbic acid on redox and endocannabinoid systems interactions in in vitro cultured human skin fibroblasts exposed to UV radiation and hydrogen peroxide. *Archiv Dermatol Res*. 2017;309:285–303.
15. Damodarasamy M, Johnson RS, Bentov I. Hyaluronan enhances wound repair and increases collagen III in aged dermal wounds. *Wound Repair Regen.* 2014;22:521.
16. Dicker KT, Gurski LA, Pradhan-Bhatt S. Hyaluronan: a simple polysaccharide with diverse biological functions. *Acta Biomater*. 2013;10:1558.
17. Buckley C, Murphy EJ, Montgomery TR. Hyaluronic acid: a review of the drug delivery capabilities of this naturally occurring polysaccharide. *Polymers*. 2022 2022;14:3442.
18. Dorf N, Maciejczyk M. Skin senescence—from basic research to clinical practice. *Front Med (Lausanne)*. 2024;11:1484345.
19. Bocheva G, Slominski RM, Slominski AT. Neuroendocrine aspects of skin aging. *Int J Mol Sci*. 2019;20:2798.
20. Löffek S, Schilling O, Franzke CW. Biological role of matrix metalloproteinases: a critical balance. *European Respiratory Journal*. 2011;38:191–208.
21. Mathew-Steiner SS, Roy S, Sen CK. Collagen in wound healing. *Bioengineering*. 2021;8:63.
22. Gardeazabal L, Izeta A. Elastin and collagen fibres in cutaneous wound healing. *Exp Dermatol*. 2024;33:e15052.
23. Yue B. Biology of the Extracellular matrix: an overview. *J Glaucoma*. 2014;23:S20.
24. Dąbrowska AK, Spano F, Derler S. The relationship between skin function, barrier properties, and body-dependent factors. *Skin Res Technol*. 2018;24:165–174.
25. Maranduca MA, Hurjui LL, Branisteanu DC. Skin - a vast organ with immunological function (Review). *Exp Ther Med*. 2020;20:18.
26. Gimeno-Lluch I, Benito-Jardón M, Guerrero-Barberà G. The role of the fibronectin synergy site for skin wound healing. *Cells*. 2022;11:2100.
27. Chen J, Liu Y, Zhao Z. Oxidative stress in the skin: impact and related protection. *Int J Cosmet Sci*. 2021;43:495–509.
28. Papaccio F, D'arino A, Caputo S. Focus on the contribution of oxidative stress in skin aging. *Antioxidants*. 2022 2022;11:1121.
29. Sanchez MC, Lancel S, Boulanger E. Targeting oxidative stress and mitochondrial dysfunction in the treatment of impaired wound healing: a systematic review. *Antioxidants*. 2018;7:98.
30. Wang Q, Chi L. The alterations and roles of glycosaminoglycans in human diseases. *Polymers*. 2022 2022;14:5014.
31. Salman S, Paulet V, Hardonnière K. The role of NRF2 transcription factor in inflammatory skin diseases. *Biofactors*. 2025;51:e70013.
32. Wroński A, Jarocka-Karpowicz I, Surażyński A. Modulation of redox and inflammatory signaling in human skin cells using phytocannabinoids applied after UVA irradiation: *in vitro* studies. *Cells*. 2024;13:965.
33. Skrzydlewska A, Antioxidative E, Aldini G. Antioxidative and anti-inflammatory activity of ascorbic acid. *Antioxidants*. 2022;11:1993.
34. Gęgotek A, Ambrożewicz E, Jastrząb A. Rutin and ascorbic acid cooperation in antioxidant and antiapoptotic effect on human skin keratinocytes and fibroblasts exposed to UVA and UVB radiation. *Arch Dermatol Res*. 2019;311:203–219.
35. Ferrada L, Magdalena R, Barahona MJ. Two Distinct Faces of Vitamin C: AA vs. DHA. *Antioxidants*. 2021 2021;10:215.
36. Wilson JX. The physiological role of dehydroascorbic acid. *FEBS Lett*. 2002;527:5–9.
37. Cisternas P, Silva-Alvarez C, Martínez F. The oxidized form of vitamin C, dehydroascorbic acid, regulates neuronal energy metabolism. *J Neurochem*. 2014;129:663–671.
38. Dewhirst RA, Fry SC. The oxidation of dehydroascorbic acid and 2,3-diketogulonate by distinct reactive oxygen species. *Biochemical Journal*. 2018;475:3451.
39. Ahmad S, Jose Da Costa Gonzales L, Bowler-Barnett EH. The UniProt website API: facilitating programmatic access to protein knowledge. *Nucleic Acids Res*. 2025;53:W547–W553.

40. Kuhn M, von Mering C, Campillos M. STITCH: interaction networks of chemicals and proteins. *Nucleic Acids Res*. 2007;36:D684.

41. Rezatofighi SE. Exogenous interactome analysis of bovine viral diarrhea virus-host using network based-approach and identification of hub genes and important pathways involved in virus pathogenesis. *Biochem Biophys Rep*. 2024;40:101825.

42. Szklarczyk D, Kirsch R, Koutrouli M. The STRING database in 2023: protein–protein association networks and functional enrichment analyses for any sequenced genome of interest. *Nucleic Acids Res*. 2022;51:D638.

43. Shannon P, Markiel A, Ozier O. Cytoscape: A software Environment for integrated models of biomolecular interaction networks. *Genome Res*. 2003;13:2498–2504.

44. Barrett T, Wilhite SE, Ledoux P. NCBI GEO: archive for functional genomics data sets—update. *Nucleic Acids Res*. 2013;41:D991–D995.

45. Compare lists - multiple list comparator - Venn diagram generator, free online tool to find set intersections.

46. Mi H, Muruganujan A, Casagrande JT. Large-scale gene function analysis with PANTHER classification system. *Nat Protoc*. 2013;8:1551.

47. Chin CH, Chen SH, Wu HH. cytoHubba: identifying hub objects and sub-networks from complex interactome. *BMC Syst Biol*. 2014;8:S11.

48. Bader GD, Hogue CWV. An automated method for finding molecular complexes in large protein interaction networks. *BMC Bioinformatics*. 2003;4:2.

49. Ge SX, Jung D, Jung D. ShinyGO: a graphical gene-set enrichment tool for animals and plants. *Bioinformatics*. 2020;36:2628–2629.

50. Kanehisa M, Furumichi M, Sato Y. KEGG: integrating viruses and cellular organisms. *Nucleic Acids Res*. 2021;49:D545–D551.

51. RCSB PDB: Homepage. 2026.

52. Berman HM, Westbrook J, Feng Z. The protein data bank. *Nucleic Acids Res*. 2000;28:235–242.

53. AlphaFold Protein Structure Database. 2026.

54. Grant OC, Wentworth D, Holmes SG. Generating 3D models of carbohydrates with GLYCAM-Web. *bioRxiv*. 2025.05.08.652828.

55. Goddard TD, Huang CC, Meng EC. UCSF ChimeraX: meeting modern challenges in visualization and analysis. *Protein Sci.* 2017;27:14.

56. Yang C, Cao M, Liu H. The high and low molecular weight forms of hyaluronan have distinct effects on CD44 clustering. *J Biol Chem*. 2012;287:43094–43107.

57. Bourguignon LYW, Wong G, Earle CA. Interaction of low molecular weight hyaluronan (LMW-HA) with CD44 and toll-like receptors promotes the actin filament-associated protein (AFAP-110)-Actin Binding and MyD88-NFκB signaling leading to pro-inflammatory cytokine/chemokine production and breas…. *Cytoskeleton (Hoboken)*. 2011;68:671.

58. Campo GM, Avenoso A, Campo S. Small hyaluronan oligosaccharides induce inflammation by engaging both toll-like-4 and CD44 receptors in human chondrocytes. *Biochem Pharmacol*. 2010;80:480–490.

59. Bahrami SB, Tolg C, Peart T. Receptor for Hyaluronan Mediated Motility (RHAMM/HMMR) is a novel target for promoting subcutaneous adipogenesis. *Integr Biol (Camb)*. 2017;9:223.

60. Lawrance W, Banerji S, Day AJ. Binding of Hyaluronan to the Native Lymphatic Vessel Endothelial Receptor LYVE-1 Is Critically Dependent on Receptor Clustering and Hyaluronan Organization. *J Biol Chem*. 2016;291:8014.

61. Jackson DG. Hyaluronan in the lymphatics: The key role of the hyaluronan receptor LYVE-1 in leucocyte trafficking. *Matrix Biology*. 2019; 78–79: 219–235.

62. Sokolowska M, Chen LY, Eberlein M. Low molecular weight hyaluronan activates cytosolic phospholipase A2α and eicosanoid production in monocytes and macrophages. *J Biol Chem*. 2013;289:4470.

63. Ruppert SM, Hawn TR, Arrigoni A. Tissue integrity signals communicated by high-molecular weight hyaluronan and the resolution of inflammation. *Immunol Res*. 2014;58:186.

64. Neumann A, Schinzel R, Palm D. High molecular weight hyaluronic acid inhibits advanced glycation endproduct-induced NF-κB activation and cytokine expression. *FEBS Lett*. 1999;453:283–287.

65. Takeda M, Ogino S, Umemoto R. Ligand-induced structural changes of the CD44 hyaluronan-binding domain revealed by NMR. *J Biol Chem*. 2006;281:40089–40095.

66. Yang B, Yang BL, Savani RC. Identification of a common hyaluronan binding motif in the hyaluronan binding proteins RHAMM, CD44 and link protein. *EMBO J*. 1994;13:286.

67. Banerji S, Hide BRS, James JR. Distinctive properties of the hyaluronan-binding domain in the lymphatic endothelial receptor Lyve-1 and their implications for receptor function. *J Biol Chem*. 2010;285:10724–10735.

68. Weigel PH, Baggenstoss BA. What is special about 200 kDa hyaluronan that activates hyaluronan receptor signaling? *Glycobiology*. 2017;27:868–877.

69. Hadarovich A, Anishchenko I, Tuzikov A V.. Gene ontology improves template selection in comparative protein docking. *Proteins*. 2018;87:245.

70. Deng D, Sun PC, Yan CY. Crystal structure of human GLUT3 bound to D-glucose in the outward-occluded conformation at 1.5 angstrom. *Worldwide Protein Data Bank*. 2015.

71. Deng D, Sun P, Yan C. Molecular basis of ligand recognition and transport by glucose transporters. *Nature*. 2015;526:391–396.

72. Crystal structure of human soluble CLIC1 with catalytic cysteine (Cys24) in sulphonic acid form. 2022.

73. Das BK, Kumar A, Sreekumar SN. Comparative kinetic analysis of ascorbate (Vitamin-C) recycling dehydroascorbate reductases from plants and humans. *Biochem Biophys Res Commun*. 2022;591:110–117.

74. Human Glutathione Transferase O1-1 C32S Mutant in Complex with Ascorbic Acid. 2012.

75. Zhou H, Brock J, Liu D. Structural insights into the dehydroascorbate reductase activity of human omega-class glutathione transferases. *J Mol Biol*. 2012;420:190–203.